QUANTIFYING METHANE FLUXES ON MARS: MODELING THE VERTICAL EVOLUTION OF MARTIAN METHANE FOR IMPROVED DETECTION AND ANALYSIS

MADELINE E. WALTERS

A THESIS SUBMITTED TO THE FACULTY OF GRADUATE STUDIES
IN PARTIAL FULFILMENT OF THE REQUIREMENTS
FOR THE DEGREE OF
MASTERS OF SCIENCE

GRADUATE PROGRAM IN EARTH AND SPACE SCIENCE
YORK UNIVERSITY
TORONTO, ONTARIO

AUGUST 2023

Abstract

Searching for the presence of biosignatures on Mars is central to understanding and discovering clues to the geological and chemical history of the planet, and may lead us to unexpected discoveries. Methane has been observed in the Martian atmosphere for several decades, however, our understanding of the behavior of methane on Mars remains limited, particularly in terms of its diurnal variations, and its sources and sinks. On Earth, methane is regulated largely by biological activity, thus the presence of methane on Mars raises the question of whether the source of Martian methane is geochemical or biogenic in origin. Measurements of methane by the Sample Analysis at Mars Tunable Laser Spectrometer (SAM-TLS) aboard NASA's Curiosity Rover have revealed a background seasonal cycle of methane, though no measurement of the full diurnal cycle have yet been made. We use global circulation model (GCM) outputs to model the diurnal vertical evolution of methane on Mars and the strength of its flux from the surface. We also look at the allowable flight temperatures (AFT) for a dedicated instrument that is able to sample the Martian atmosphere hourly at sub-ppbv levels to better characterize the Martian methane cycle. The precision of such an instrument relies on the cooling of the gas sample, which must be kept free of condensing water vapor. Therefore, we look at the variability of the water frost point which reveals the areas of the Martian surface at which the instrument is most sensitive.

Acknowledgements

I would like to first thank my supervisors, John and Mark, for being wonderful advisors and giving me the opportunity to study something I'm passionate about. I'm incredibly lucky to have gotten to work with you both and I have been able to grow so much as a researcher and scholar under your supervision.

Thank you to the wonderful PVL group - you've all been great support through my degree and I thank you for your patience and helpfulness when I frantically message about LaTeX or clouds at 2:00am. I would next like to give a special thanks to my seventh grade math teacher, Ms. Hale, for helping me to get into math and science. Your talent for inspiring students to love a subject that most are taught to be wary of is a big reason I am here.

Of course a huge thank you to my wonderful friends, without whom I absolutely would not have made it through the last few years. Wes - your love and friendship, and occasional boba have kept me afloat and you always manage to put a smile on my face even on the roughest days. Anna and Adiv - I will always cherish our midnight talks, dinners, and time we've spent together. Thank you to Natalie and Ayushi for always making me laugh and for sharing special interests with me. Thank you all for all of your support and kindness and for making me feel so at home here.

Finally I would like to thank my parents, for all the unconditional love and support you've given me. I would not have gotten here without you - I love you.

Table of Contents

List of Tables

List of Figures

Chapter 1

Introduction

1.1 Introduction to the Martian Atmosphere and Planetary Boundary Layer

The composition of the Martian atmosphere is vital for understanding the planet's surface interactions, and can provide valuable insights into the physical processes that are essential for studying the planet. The Martian atmosphere is composed primarily of carbon dioxide (95.3%), nitrogen (2.6%), and argon (1.9%), as well as trace gases, such as oxygen, carbon monoxide, water vapor, and methane (Williams, 2023). Seasons on Mars are indicated by solar longitudes (L_s), which correspond to the angle of Mars in its orbit relative to the sun, measured from the line linking to Mars on the spring equinox at L_s=0° and moving counterclockwise as viewed from above the Sun's north pole. L_s= 90°, 180°, and 270° thus refer to northern summer solstice, northern autumn equinox, and northern winter solstice respectively (Fig. 1.1).

From L_s=0° to 360°, the planet makes a full orbit around the sun, which takes 668.6 sols (Mars days), where one sol is approximately 24 hours and 39 minutes. Mars

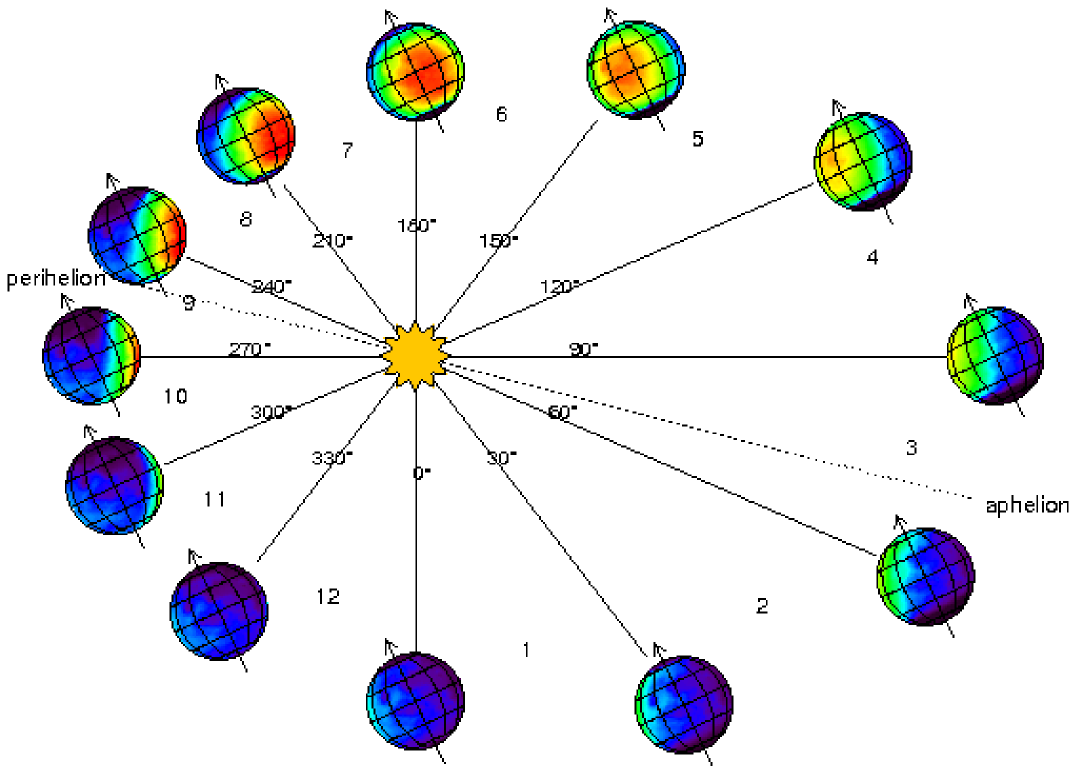

Figure 1.1: Solar longitudes of Mars (**Fig. 2a**; Bhattacharyya et al., 2015). The angle around the sun is measured from the line linking to Mars on the vernal equinox, and each season is represented by a 90° change starting at northern spring equinox (L_s=0°). During perihelion, the southern hemisphere experiences increased heating, promoting increased planet-wide dust storms from L_s=180° to L_s=360° (Kok et al., 2012).

has an obliquity of 25.19°, such that the four seasons on Mars are relatively similar to those on Earth, which has an obliquity of approximately 23.5°. Additionally, Mars has a high orbital eccentricity of 0.093 (compared to Earth's 0.017), which results in higher solar radiation and stronger heating of the surface during southern summers at perihelion (L_s= 250°) when the planet is closest to the sun, relative to northern summers. During southern summer, increased heating creates temperature gradients and atmospheric instability, promoting the formation of global dust storms and dust devils (Wang et al., 2023).

Relative to Earth, which has a standard sea-level atmospheric pressure of approximately 1013 millibars (mb), the Martian atmosphere is extremely thin, with an average surface pressure of approximately 6.1 mb (Haberle, 2015). The surface pressure varies with location and time of year, ranging over a factor of 15 due to the variations in topography, and changing by approximately 30% seasonally, and 10% daily. During northern autumn and winter, the north ice cap grows with CO_2 as temperatures cool, causing a decrease in pressure. This decrease in pressure also occurs during southern winter, when the south polar ice cap grows. As the ice caps begin to sublimate, the atmosphere then thickens with CO_2, causing an increase in pressure (Hess et al., 1980; Hu et al., 2012).

At the lowest layers of the atmosphere, near the planet's surface (Fig. 1.2a), the temperature is strongly influenced by the diurnal (daily) and seasonal variations. Globally, temperature decreases with increasing altitude (Fig. 1.2b), which is a typical condition for planets with a predominantly transparent atmosphere. However, temperature inversions can occur, where temperature begins to increase with height, inhibiting mixing. During the daytime, the surface is heated by solar radiation and increased mixing can occur due to convection, while at night the surface cools rapidly through radiative cooling, decreasing the temperature. Temperature can play a

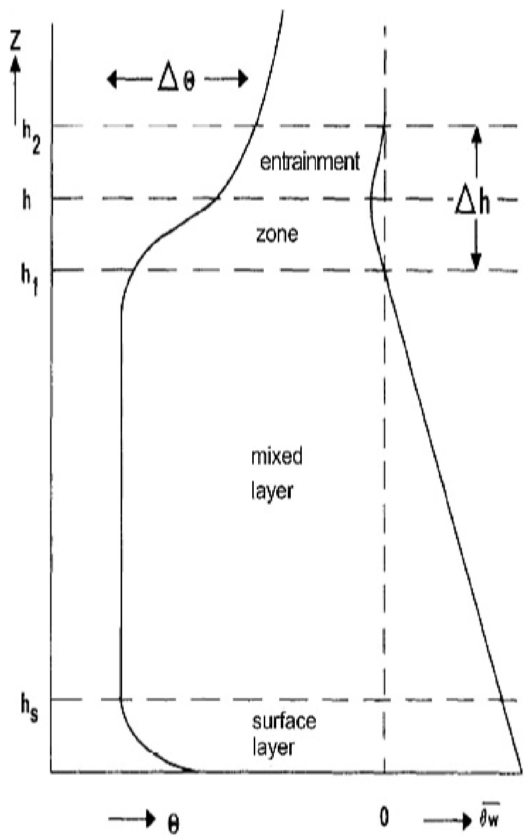

(a)

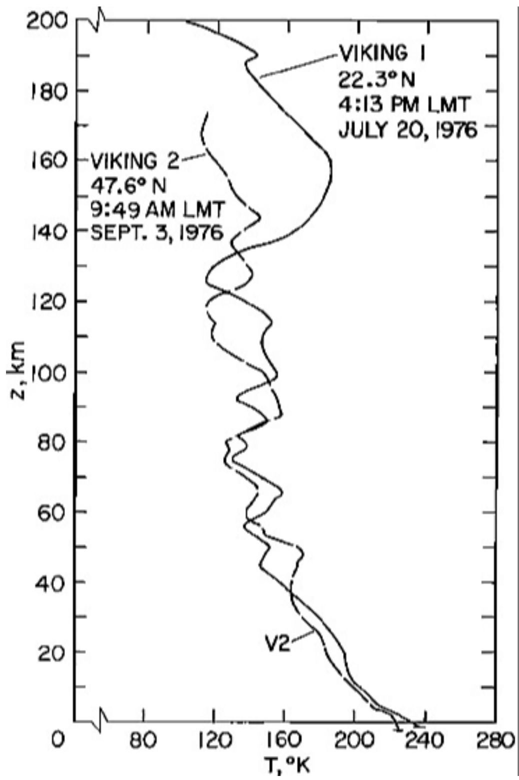

(b)

Figure 1.2: From Petrosyan et al. (2011). (a) Structure of the planetary boundary layer (PBL) during the day. The vertical heat and momentum fluxes in the surface layer are almost independent of height. The mixed layer above the surface layer is where the majority of the mixing in the PBL (here h is PBL height) occurs up to the top of the PBL, which is characterized by a jump in potential temperature ($\Delta\theta$). (b) Temperature profiles measured by the Viking 1 and 2 spacecraft.

significant role in surface interactions and processes, affecting mixing and weather phenomena. The portion of the atmosphere closest to the surface is referred to as the planetary boundary layer (PBL). This refers to the lowest part of the atmosphere where surface-coupled highly convective interactions take place (Read et al., 2017).

The height of the PBL increases to approximately 5-10 km during the day, when the surface is heated by the sun and convective mixing can occur (Petrosyan et al., 2011). Overnight, the PBL collapses down to a few meters where a stratified layer is formed and convection is inhibited. Atmospheric turbulent mixing also reaches a minimum in this layer overnight, and chemical tracers such as methane are able to build up without mixing (Moores et al., 2019b).

The PBL is important for studying surface exchanges of heat, wind, water, and trace gases in the atmosphere. Compared to the PBL on Earth, the Martian PBL is much less dense, which can impact mass fluxes and the exchanges of heat and momentum. At the surface, heat transfer is driven mainly by solar radiation, and momentum transfer is driven by wind shear and buoyancy, resulting in convective plumes and turbulent eddies, which drive turbulent diffusion of atmospheric constituents. This thesis will focus primarily on the processes within the PBL that drive the diffusion of trace gases in the atmosphere.

1.2 Martian Methane Detection

1.2.1 Sources of Methane on Mars

During the Noachian period, approximately 4.1 to 3.7 billion years ago, Mars is believed to have had an abundance of surface water (Fassett & Head, 2008), potentially making it a habitable environment for microorganisms. However, despite extensive exploration and research, no evidence of life, either in past or present conditions, has

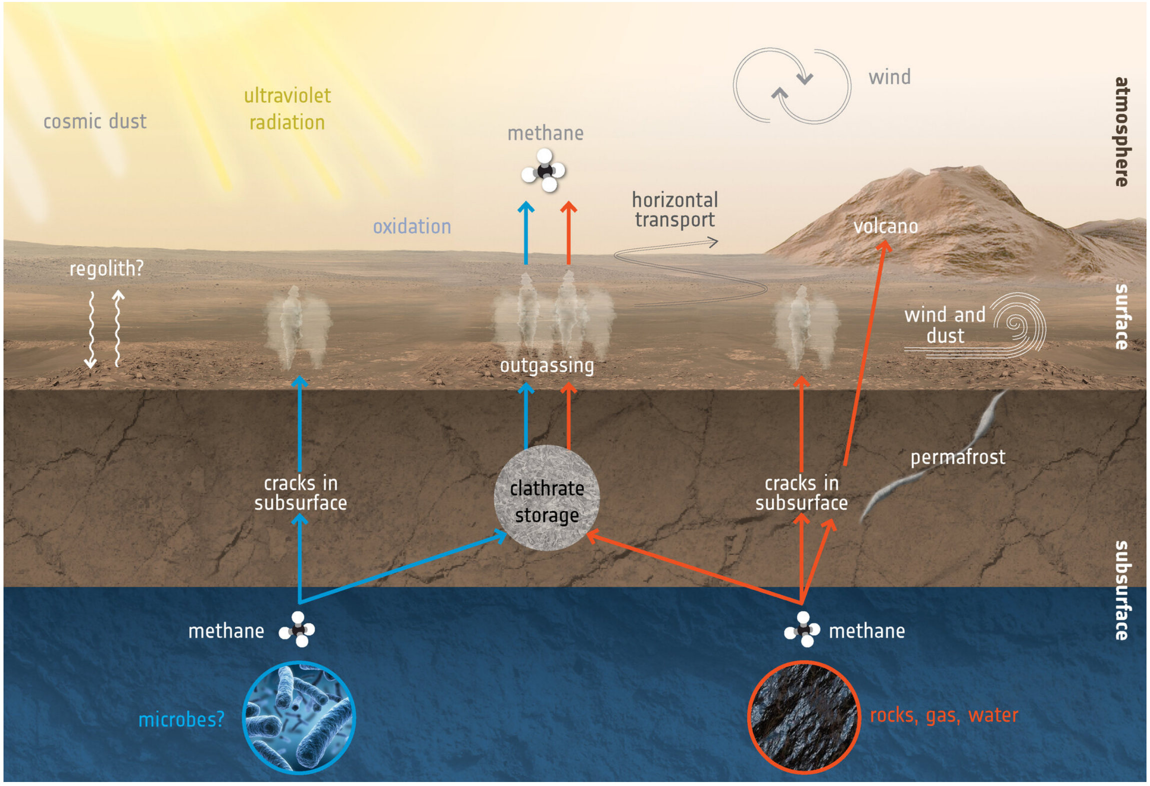

Figure 1.3: Possible sources and sinks of methane on Mars. Potential sources include microbes, release from clathrate storage, UV degradation, regolith adsorption, and other subsurface interactions. Image credit: NASA/JPL/SAM-GSFC/U. Michigan

been found on Mars. Nevertheless, the search for life on Mars remains a topic of great astrobiological interest.

Methane on Earth is primarily generated by mostly by biogenic sources (Cicerone & Oremland, 1988), notably microbial activity. Additionally, geological processes also contribute to methane emissions (Fig. 1.3). Therefore, the detection of methane on Mars carries significant implications as it could offer valuable insights into both present and past microbial activity on the planet, while also enhancing our understanding of its geological history. In addition to potential biogenic sources, nonbiogenic sources of methane on Mars may include ultraviolet (UV) interaction with organic materials from interplanetary dust particles (IDPs) and comet dust (Sandford, 2008), or interactions between subsurface water and olivine (Oehler & Etiope, 2017). The latter occurs when water and CO_2 interacts with olivine, a magnesium iron silicate, and causes a reaction in a process called serpentinization, forming hydrogen and methane (Klein et al., 2019). Other possible sources of methane include subsurface reservoirs such as clathrate hydrates, a form of crystalline water ice that can store and release trapped ancient methane into the atmosphere (Chassefière, 2009). Clathrates would explain a source of sporadic methane release, with stability conditions currently met in the shallow subsurface, though further geological analysis is required in order to gain a more accurate estimation on where sufficient methane supplies could exist (Gloesener et al., 2021).

1.2.2 Methane Measurements

In 1999, ground-based telescope observations from the Canada-France-Hawaii Telescope (CFHT; Krasnopolsky et al. (2004)) suggested a global methane mixing ratio average of 10 ± 3 parts per billion by volume (ppbv) on Mars. In 2003, the NASA Infrared Telescope Facility (IRTF) observed ~ 45 ppbv near the equator, though that was followed by subsequent non-detections (Mumma et al., 2009). Since then, orbiters and landers have focused on detecting and measuring methane in the Martian atmosphere to gain a better understanding of the distribution and behaviour of the gas. Initial claims of high abundances have since been reduced as instrument sensitivity and accuracy have improved. Though there have been many measurements of methane, none had shown a repeatable spatial or diurnal trend. In 2004, the Planetary Fourier Spectrometer (PFS) onboard the European Space Agency's (ESA) Mars Express orbiter (Formisano et al., 2004) detected a mixing ratio of 10 ± 5 ppbv from averaged global data using mostly nadir pointing (Geminale et al., 2008).

Since 2012, the Sample Analysis at Mars Tunable Laser Spectrometer (SAM-TLS) onboard the Curiosity rover as part of the Mars Science Laboratory (MSL) mission

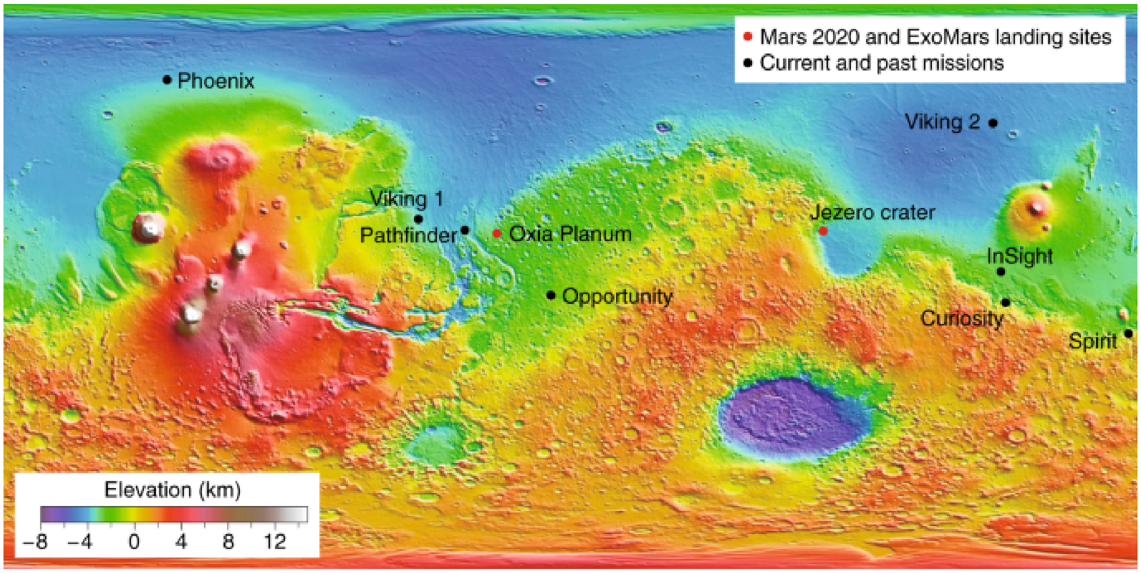

Figure 1.4: Topographic map of Mars showing the locations of Mars lander and rover sites. The Curiosity rover is located at 4.5°S, 137.4°E in Gale Crater. Source: Topographic map is created with Mars Orbiter Laser Altimeter (MOLA; Smith et al. (2001)); Image is by Lakdawalla (2019).

(Mahaffy et al., 2012) has taken nighttime measurements of methane in Gale Crater, which is situated slightly south of the equator at 4.5°S, 137.4°E (Fig. 1.4, 1.5). SAM-TLS initially reported a low methane abundance of 0.18 $\pm$ 0.67 ppbv with an upper limit of 1.3 ppbv (Webster et al., 2013). Subsequent observations taken over a 20-month period reported a background level of 0.69 $\pm$ 0.25 ppbv, with occasional spikes of up to 7.2 $\pm$ 2.1 ppbv (Webster et al., 2018).

Two methods of atmospheric ingestion were used: the first is a direct ingest method, where gas directly from the atmosphere fills a chamber called a Herriott cell. Within the Herriott cell, a laser set to a precisely tuned wavelength is reflected between mirrors through the gas for $\sim$ 20 minutes, yielding an uncertainty of approximately $\pm$ 2 ppbv. The second method uses gas enrichment to scrub the atmospheric CO_2 from the sample, enriching the methane abundance by a factor of $\sim$ 25, which reduces the uncertainty to approximately $\pm$ 0.1 ppbv, but requires approximately six times as

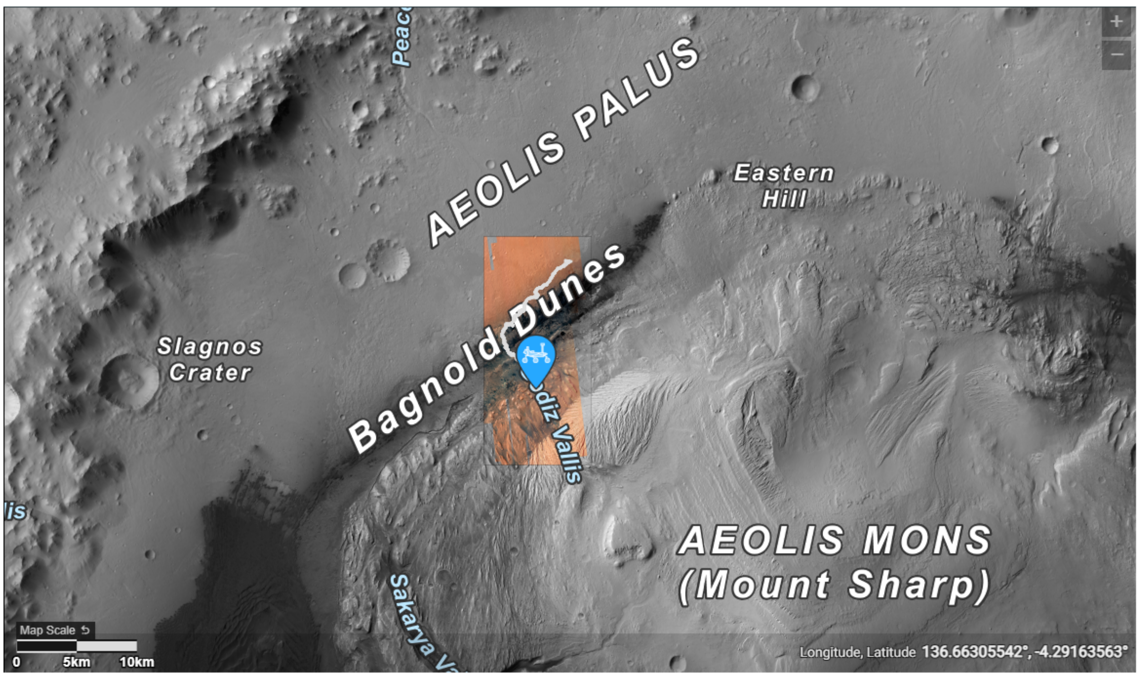

Figure 1.5: Location of the Curiosity rover and its path in Gale Crater. Both the greyscale map and true-color base map are created with image data from the Context and HiRISE cameras on NASA's Mars Reconnaissance Orbiter (Malin et al., 2007; McEwen et al., 2007). Image credit: "NASA Curiosity Location Map" (2021) Available online https://mars.nasa.gov/maps/location/?mission=Curiosity.

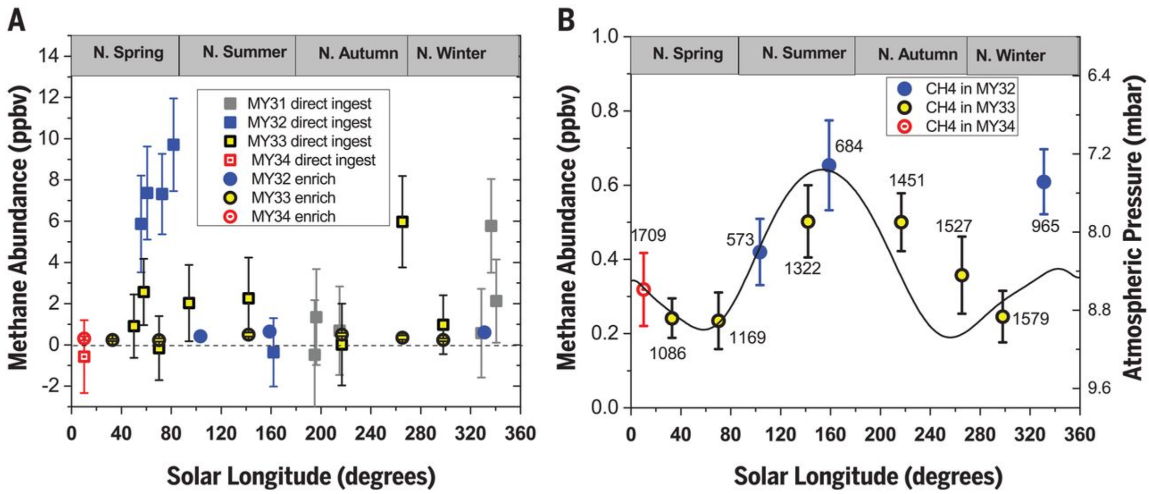

Figure 1.6: From Webster et al. (2018), Fig. 1. SAM-TLS methane measurements versus solar longitude. (a) All methane measurements up to May 2017, including background abundances and spikes of up to $\sim$ 10 ppbv using both direct-ingest and enrichment run methods. (b) Background abundances from only the enrichment run method. A seasonal variation is shown, with the maximum in northern summer.

much time to complete. The latter method is used to more effectively determine the background abundance of methane, which has been shown to vary with season (Fig. 1.6b). During northern summer, the background abundance reaches a maximum, then decreases during northern autumn, slightly increasing again at the end of northern winter. Figure 1.6a shows all values from both direct and enrichment runs, which includes background values averaging to $\sim$ 0.41 ppbv and spikes of up to $\sim$ 10 ppbv (Webster et al., 2018).

In 2013, SAM-TLS detected a methane spike of 5.78 $\pm$ 2.27 ppbv at Gale Crater (Webster et al., 2013; Webster et al., 2015). One day after this measurement, PFS detected a 15.5 $\pm$ 2.5 ppbv spike over Gale Crater from its position in orbit, though no spikes were detected in any other orbital passes (Giuranna et al., 2019). This correlation between SAM-TLS and PFS was the first case of independent atmospheric methane measurements (Table 1.1).

Table 1.1: Methane measurements taken by PFS and SAM-TLS from sol 304 to 318 during MSL mission, retrieved from (Giuranna et al., 2019)

Sols relative to SAM-TLS measurements	Sols since MSL landing	Local True Solar Time (LTST)	Value (ppbv)	Instrument
-1	Sol 304	$\sim$ 9:45 (LTST)	$\lesssim 3$	PFS
0	Sol 305	13:00 (LTST); ingestion: 20 minutes	5.78 ± 2.27	SAM-TLS
1	Sol 306	9:41 (LTST); measurement duration: 43 minutes	15.5 ± 2.5	PFS
8	Sol 313	NA	2.13 ± 2.02	SAM-TLS
11	Sol 316	$\sim$ 9:24 (LTST)	$\lesssim 5$	PFS
13	Sol 318	$\sim$ 9:19 (LTST)	$\lesssim 5$	PFS

1.2.3 Measurement Discrepancies and Methane Destruction

In 2016, the Atmospheric Chemistry Suite (ACS) and Nadir and Occultation for Mars Discovery (NOMAD) instruments onboard the ESA-Roscosmos ExoMars Trace Gas Orbiter (TGO) were sent to gather additional measurements of atmospheric methane to help assess the origin of the gas. These instruments took highly sensitive measurements of the Martian atmosphere, though in 2018 they reported no methane over a range of latitudes in both hemispheres (Korablev et al., 2019). TGO obtained an upper limit for methane of 0.05 ppbv, which is significantly lower than previous reported measurements (Fig. 1.7). One major difference in TGO's measurement strategy compared to SAM-TLS is the time of day the measurements take place. SAM-TLS takes methane measurements at around midnight when mixing is limited and methane builds up to detectable levels, compared to daytime nondetections (Webster et al., 2021). However, TGO makes measurements using sunlight to detect methane starting approximately 5 km above the surface, which is during the daytime when the atmosphere exhibits more turbulent mixing, and thus methane is mixed away to undetectable concentrations.

Based on the current understanding of the Martian atmosphere, the calculated photochemical lifetime of methane in the Martian atmosphere is nearly 300 years (Wong et al., 2003) before being oxidized or destroyed by photolysis. However, the non-detections by TGO indicate that in order to avoid high-altitude methane accumulation, rapid destruction or sequestration of methane must occur. Korablev et al. (2019) calculates that if methane was being continuously emitted from Gale Crater and accumulating globally, then the source could only have been emitting for at most 24 Martian years before TGO limits could be reached. Furthermore, to explain the rapid variations in methane reported by Webster et al. (2018), the methane lifetime should be even shorter, down to one year or less (Lefèvre & Forget, 2009).

Several additional destruction mechanisms have been proposed that could explain the fast removal of atmospheric methane. One possible explanation is that perchlorate salts, which can be found in Martian dust, can rapidly oxidize methane when activated by UV radiation (Zhang et al., 2022). Additionally, laboratory studies have shown that saltation of dust particles, where strong wind near the surface forces dust to move in jumps, builds charge in dust grains and can ionize surrounding gas molecules including methane. This induces a process known as triboelectric charging, which could potentially lead to the removal of any methane signatures (Atreya et al., 2006) (Thøgersen et al., 2019). However, evidence of active triboelectric discharge has not yet been detected despite detailed investigations (Sapers et al., 2021a).

The sources and sinks of Martian methane remain uncertain; however, the observed seasonal and diurnal variation in the background methane mixing ratio can be explained by subsurface release consistent with the adsorption onto and diffusion through regolith, and subsequent near-surface mixing (Moores et al., 2019a). Once

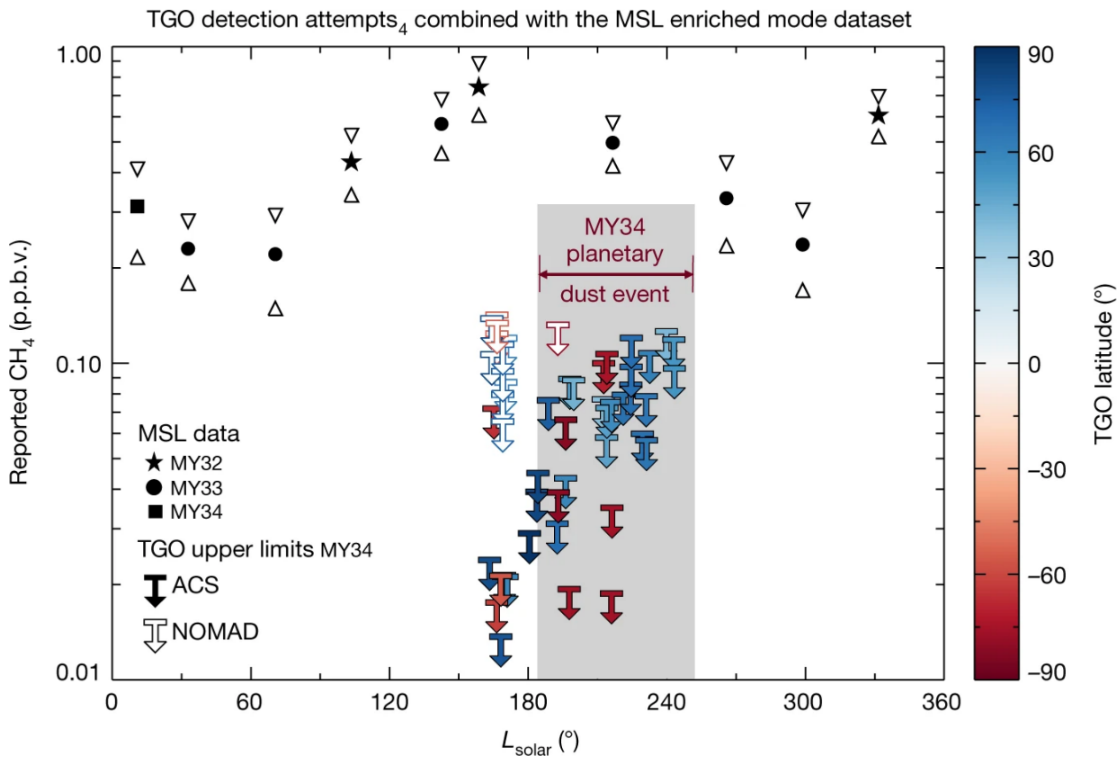

Figure 1.7: TGO detection attempts and Curiosity enrichment run results. The upper limits obtained by TGO are compared to the seasonal background variation measured by SAM-TLS (Korablev et al., 2019).

methane is released from the surface after diffusing through regolith, mixing within the PBL can quickly distribute methane such that any localized concentrations become greatly reduced. Assuming planet-wide uniform seepage of methane, current flux estimates range from 2×10^{-11} kg km^{-2} s^{-1} to 8.4×10^{-9} kg km^{-2} s^{-1}, based on modeled upper-limit estimates of microseepage from Gale Crater (Formisano et al., 2004; Moores et al., 2019a). If Gale Crater alone is not an isolated source of methane on Mars, and methane is accumulating and mixing globally, combined with the lack of detection by TGO, it implies the existence of a process that quickly removes methane from the lower atmosphere. This process prevents the widespread dispersion of methane globally and points towards a mechanism of destruction or sequestration.

Giuranna et al. (2019) suggests that because the observed methane detected by

PFS corresponds to an estimated quantity of approximately 39-54 tons within an observed area of $\sim$ 46,000 km^2 from the orbit, this observation, paired with the SAM-TLS observation, indicates that the emission occurred from outside of Gale Crater. To identify a potential source region, methane transport was simulated using the Global Environmental Multiscale (GEM)-Mars general circulation model (GCM; Neary and Daerden (2018) and Viscardy et al. (2016)). The GCM incorporated methane emission patterns, including temporal variation, and revealed a potential source region located east of Gale Crater (Giuranna et al., 2019). Additional constraints provided by the observation suggest that the emission occurred on a short timescale and not far from Gale Crater. Further investigations have been conducted to study the horizontal transport of methane and analyze backward trajectories to identify potential source regions. Factors such as wind patterns, gas flux, and methane abundance play a role in determining possible source locations. In a study by Luo et al. (2021), back trajectory modeling, which maps out upstream emissions, was used to identify regions where the methane spikes observed by SAM-TLS may have originated. The analysis revealed that methane spikes are likely sourced by surface emissions nearby in northwestern Gale Crater, assuming the methane photochemical lifetime of $\sim$300 years. However, this problem remains weakly constrained due to limited knowledge about the precise source locations, initial timing and duration of the emissions, and the strength of the methane fluxes that characterize the release pattern. Further measurements that can capture hourly processes, coupled with modeling using GCMs, could further improve potential source location identification for methane spikes.

1.3 Martian Atmospheric Gas Evolution Experiment

1.3.1 The Methane Cycle

Methane concentration measurements from multiple instruments, such as the PFS on Mars Express and SAM-TLS, have shown variations in methane concentrations over different seasons (Korablev et al., 2019; Webster et al., 2018). However, due to instrument limitations such as sensitivity, and the limited number of observations, it is difficult to determine the precise details of the diurnal cycle of methane on Mars. Additionally, the exact sources and sinks of methane on Mars are still a topic of active research and debate. Apart from the independent confirmation of a methane spike reported by SAM-TLS and PFS, there have been no other cases of simultaneous or near-simultaneous measurements. As such, there is a need for more frequent measurements of methane, which would provide valuable data to enhance our understanding of the Martian methane cycle, and also improve the accuracy and reliability of models.

These measurement requirements can be effectively fulfilled using a highly sensitive instrument that can sample the Martian atmosphere at hourly intervals, and provide measurements at sub-ppbv concentrations (Moores et al., 2021; Sapers et al., 2021b). Using numerical models such as a GCM to better characterize these surface interactions with methane and its diurnal cycle could further help provide insights into the sources and sinks of methane on the planet and further our understanding of the potential for current or past microbial life on Mars. Using modeling techniques can help identify how methane emissions are diffused, and inform the future design of instruments and sampling strategies for detecting and measuring methane on the Martian surface. Additionally, understanding the diurnal cycle of methane can help improve the accuracy and sensitivity of methane detection instruments, which is

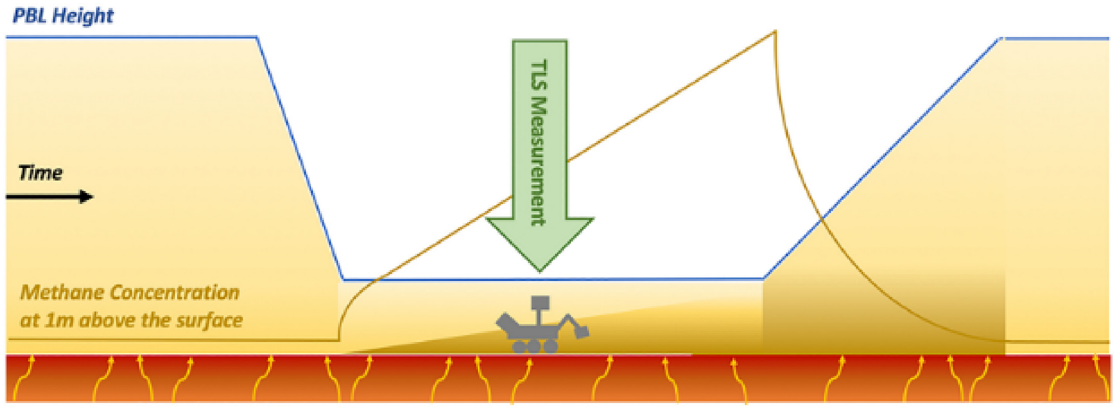

Figure 1.8: Diurnal methane evolution versus PBL height, starting at local noon when the PBL is at or near maximum height and mixing occurs. Through the night, the PBL collapses down to tens of meters and mixing is inhibited, allowing methane to build up (Moores et al., 2019b).

crucial for future missions aimed at searching for signs of current or past microbial life on Mars. Because SAM-TLS makes measurements at night when methane is building up to greater concentrations (Fig. 1.8), having an instrument capable of taking high frequency measurements throughout an entire sol would be able to address some of the uncertainties in our current models, and create a better understanding of the methane cycle (Sapers et al., 2021b; Webster et al., 2021).

The Martian Atmospheric Gas Evolution (MAGE) experiment aims to develop an instrument capable of measuring methane at sub-ppbv levels and would be able to detect higher spikes and their subsequent decay. This instrument is designed to make hourly measurements, as well as measure the background seepage and diurnal cycle of methane without the need for enrichment. However, the background methane seepage and episodic releases that would be observed by this instrument are poorly understood, which introduces uncertainties into the predicted quantities MAGE is expected to measure.

As such, an instrument like the MAGE instrument would benefit from being deployed in an area such as Gale Crater or other locations similar to Gale where conditions are conducive to the potential emission, accumulation, and detection of methane. Other locations of Mars that may be ideal candidates for such an instrument include areas that have hydrated minerals and evidence of past water activity that may either promote serpentinization or the preservation of organic materials from IDPs. Furthermore, regions directly outside of Gale Crater may also be good candidates for instrument deployment if emissions are being transported horizontally into Gale from outside of the crater.

Currently, our knowledge of the vertical evolution of methane on Mars is limited, and utilizing surface emission flux modeling can help identify areas of active methane release and investigate the underlying processes driving these emissions. This thesis tests theoretical calculations of methane surface fluxes as well as the predicted diurnal vertical behavior of methane using GCM outputs coupled to a 1D diffusion model.

1.3.2 Allowable Flight Temperatures

Because of the limitations on methane sampling on Mars, an instrument is needed for more precise and frequent measurements capable of sampling Martian methane at levels consistent with sub-ppbv concentrations. As part MAGE, a model instrument in development for this purpose is a high-sensitivity spectrometer that relies on photons reflecting thousands of times between highly reflective mirrors to generate absorption pathlengths that are kilometers long. This instrument, known as the Off-Axis Integrated Cavity Optical Spectrometer (OA-ICOS), is currently being developed by ABB Inc. in Québec, Canada (Fig. 1.9). The OA-ICOS is a compact and robust spectrometer specifically designed to meet the demands of such precise measurements, including the detection of lower concentrations resulting from background microseepage.

Figure 1.9: The ABB Inc. OA-ICOS instrument, which is attached to a hexacopter. This instrument is compact and robust, allowing for easy deployment and operation when taking highly sensitive measurements of methane. The instrument will be developed for the Martian climate and will be able to reliably detect sub-ppbv measurements of methane on Mars on an hourly scale.

The absorption spectrum of trace gas species is enhanced when cooling the gas sample. However, should any atmospheric volatiles condense within the gas cell, the highly-reflective mirrors may become marred, drastically cutting down the effective optical path length. In the Martian atmosphere, the first volatile to condense is typically water vapor, thus understanding the variability of the water frost point is essential for determining the performance limit of any optical instrument such as the MAGE spectrometer to ensure the maximum precision of methane measurements.

The presence of water ice on the surface of Mars presents a limitation for instruments such as gas analyzers which rely on low temperatures for higher precision. On Mars, water cannot remain in the liquid phase due to the current conditions of low pressure and temperature, which are on average $\sim$ 650 Pa and 210 K respectively, compared to the Earth averages of $\sim$ 101,300 Pa and 287 K (Bibring et al., 2006;

Carrozzo et al., 2009). Though there may be areas in which the conditions are favorable for liquid water to exist, over most of the Martian surface deposition of frost occurs directly from water vapor (Haberle et al., 2001). As increasingly sensitive instruments are developed for gas intake analysis, it is critical to address the issue of condensing water vapor within the analyzer cells. During an episode of frost, the analyzer chamber instruments would be prevented from working properly and the frost could permanently mar the optics, decreasing the precision of the instrument. As an example of the type of instrument that will be used, we use the OA-ICOS instrument being developed at ABB Inc. Achieving optimal performance of the instrument requires a comprehensive understanding of the temperatures at which water vapor condenses. We thus look at different locations on the Martian surface where such an instrument would be able to cool down to low temperatures and still remain free of condensing water vapor.

The temperature at which water condenses on the Martian surface varies both daily and seasonally (Christensen et al., 2001; Schorghofer & Edgett, 2006; Smith, 2002) This limits the temperature at which instruments such as the ABB spectrometer can operate with maximum precision without the risk of water condensing within the analyzer cell. Mapping the frost point maximums over a Martian year thus shows how the maximum precision of the instrument can be achieved, while also constraining the areas on the surface of the planet where the instrument can operate at the coolest temperature. The minimum temperature at which the instrument can operate safely and achieve the highest sensitivity without the risk of frost is the maximum frost point temperature. If the instrument is operated at a cooler temperature, condensation may occur, therefore the maximum sensitivity is achieved when the instrument is operating at or above the maximum frost point temperature.

The leading factor that drives the deposition of water frost is the water vapor content in the atmosphere. From the water vapor pressure retrieved from Thermal Emission Spectrometer (TES) observations, Schorghofer and Edgett (2006) calculated a frost point of 193 K for an annual mean partial pressure of 0.06 Pa on the surface, which would vary based on local conditions. A lower partial pressure would decrease this temperature, such that with a partial pressure of 0.01 Pa, a frost point temperature of 183 K is expected (Schorghofer & Edgett, 2006). The presence of high latitude frost shows areas on the surface which may be more susceptible to condensation as well, such as the south pole and extending up north to Hellas Planitia (Briggs et al., 1977; James et al., 1992), where the topography strongly controls the areas at which water condenses (James et al., 2001).

1.4 Motivation of Thesis

The work in this thesis seeks to use a one-dimensional diffusion model with inputs from a global climate model (GCM) to characterize the diurnal vertical evolution of methane on Mars. By using these techniques, along with measurements taken by SAM-TLS, the flux required to reproduce these measurements can then be found. Despite the numerous measurements of methane in the Martian atmosphere, uncertainties still persist regarding its sources and sinks. SAM-TLS has given insight into the background microseepage of methane along with independent spikes of higher abundances, though discrepancies between different instruments are still present, and the diurnal vertical evolution of methane has yet to be fully characterized. As such, models that better portray how methane behaves in the PBL can be used to give a more accurate depiction of the surface interactions of the gas within the Martian atmosphere and can be extended to use in future missions. By comparing numerical results to observational data, we can predict how methane will behave under different environmental conditions. Furthermore, because no measurements have been made of the entire diurnal cycle of background microseepage, having model results of this cycle along with modeled fluxes based on observational measurements will help to estimate the diurnal patterns of microseepage and gain a better understanding of the behavior of methane in the atmosphere.

The work presented in Chapter 2 will explore this diurnal variation in atmospheric methane and the results will explore the following questions:

- How does methane evolve vertically in the lower planetary boundary layer over a diurnal and seasonal time period given a constant volume flux at Gale Crater?
- What surface fluxes are needed to reproduce the concentrations recorded by SAM-TLS with global climate models and how do model results compare to fluxes estimated using a parameterized mixing layer height (Moores et al., 2019b)?
- How can we use observational data to validate model results and extend them to create a more realistic depiction of the vertical propagation of methane?

The work presented in Chapter 3 will explore the maximum temperatures at which water vapor will condense on the Martian surface with respect to a model instrument being prepared for a future mission to Mars. Due to extreme conditions on the surface, the formation of frost within an instrument is an issue that needs to be addressed in order to ensure maximum precision. This section will review and attempt to answer the following questions:

- What are the allowable flight temperatures at which a gas analyzer instrument that relies on cold temperatures for higher precision is optimized without the risk of water frost?

- Which locations and times of year on the surface are ideal for more precise measurements given the water frost point?

Chapters 4 and 5 will cover the conclusions of the work presented in Chapters 2 and 3, as well as potential future work based on these results and their implications.

Chapter 2

Diffusion Modeling For Methane Surface Flux

2.1 Methods

Two atmospheric models were employed to investigate the vertical transport of methane in the Martian atmosphere given an initial surface emission flux (see Walters, 2023 for code availability). The first model, GEM-Mars, is a 3D general circulation model (GCM) of the Martian atmosphere which uses atmospheric parameters including surface temperature, pressure, and eddy diffusion coefficients to demonstrate the effects of near-surface processes on methane (Neary & Daerden, 2018). GEM-Mars is based on the Global Environmental Multiscale (GEM) weather forecast model used for weather forecasting in Canada, and was selected because of its relevance to studying physical and chemical processes in the Martian atmosphere, as well as its accessibility and availability. The second model is a one-dimensional vertical diffusion model (VDM). The VDM uses temperature, pressure, and diffusion coefficients provided by GEM-Mars to simulate the vertical diffusion of methane from the surface, and outputs methane mixing ratios given a specified surface flux. This flux describes the source or sink strength of methane out of the surface and can provide context to the scale at which methane is accumulating on the planet. We use the methane mixing ratios from the VDM outputs to determine the surface fluxes of methane, considering the methane mixing ratios observed by SAM-TLS.

2.1.1 1D Model for Producing Methane Concentration

A one-dimensional vertical diffusion model (VDM) was used to reproduce methane mixing ratios for the lower portion of the PBL given a surface flux in parts per billion by volume per minute (ppbv $\min^{-1}$). This model is described in detail in Makar et al. (1999) and Stroud et al. (2005), where it is used to model canopy-scale trace gas evolution on Earth, and has been altered to represent the atmosphere of Mars for this study. We use no chemical reactions, differing from the studies done on Earth where atmospheric chemistry was represented by a chemical operator. The model uses the Crank-Nicholson scheme to solve the following system of equations:

$$\frac{\partial C_j}{\partial t} = E_j + \frac{\partial}{\partial z}(K(z_j)\frac{\partial C_j}{\partial t}) \tag{2.1}$$

Where C_j is the concentration of the chemical species in the j^{th} model layer, t is the timestep (1 s), K(z_j) are the eddy diffusion coefficients. Both C and K change every $1/48^{th}$ of a sol (half-hour) and vary with height. The eddy diffusion coefficients are obtained from GEM-Mars, which is described in section 2.1.2. The height (z) ranges up from the surface to 3 km in 1-m intervals. We assume that methane diffusion is most active between the surface and 3 km within the PBL, which is consistent with Gale Crater PBL depths modeled by Fonseca et al. (2018). E_j is the species' rate of change due to emissions into the jth model layer and is the optimized variable in the VDM. E_0 is emission flux at the surface for this study, treated as a lower boundary condition in the diffusion solver (Stroud et al., 2005), and is equal to 0 at all subsequent heights (1-3001 m). This term is used to compute the mass of methane entering each model layer, which is tracked in the model as molecules m^{-2} s^{-1} and later converted to kg m^{-2} sol^{-1}. The last term of the equation describes the diffusion flux, which transfers the mass of methane through each model layer, parameterized by eddy diffusion coefficients to allow for transport by turbulent mixing in the PBL. The VDM outputs methane concentrations at intervals of $1/48^{th}$ of a sol based on the diffusion coefficient intervals. To avoid methane accumulation because there is no removal mechanism, the concentration at the top of the model is set to zero. This choice is based on measurements indicating negligible methane levels at high altitudes (Korablev et al., 2019). This also is set to avoid any artificial constraints on the accumulation of methane during subsequent model runs and allows the model to simulate the natural behavior of methane transport and distribution, reflecting the observed conditions where methane concentrations are minimal or undetectable at higher altitudes on Mars.

2.1.2 GEM-Mars

GEM-Mars is a 3D GCM extending from the surface to a height of approximately 150 km, simulating Mars-specific physics within the atmosphere (Neary & Daerden, 2018). This section describes how diffusion coefficients (K values) are generated by GEM-Mars.

GEM-Mars uses 103 unevenly spaced thermodynamic levels (for temperatures and tracers), and 102 momentum levels (for horizontal winds) that resolve the atmospheric processes in and above the planetary boundary layer. The height of the lowest atmospheric level is 2 m, the next is 13 m, and spaces between levels increase with height such that near the top of the model, spacing is approximately 3 km (Fig. 2.1). Boundary conditions are derived from Mars Orbiter Laser Altimeter (MOLA) topography, which provides information on surface features.

A semi-Lagrangian advection scheme is used, where at every time step the parcel origin is calculated. Additionally, at every model grid point, reaction rates are calculated using the model temperature, pressure, and concentrations as input. GEM-Mars uses a horizontal grid resolution of $4^\circ \times 4^\circ$ (i.e. latitudinal spacing of 237 km, longitudinal spacing of 237 km at the equator and 73 km at 72° latitude), and has an integration time step of $1/48^{th}$ of a sol (approximately each half-hour of a Martian day). GEM-Mars has been updated to include parameterizations such as those used for active dust lifting, radiatively active water ice clouds, and non-condensable gas enrichment. The model was used to show that surface emissions of methane can result in a highly nonuniform vertical distribution through the atmosphere, and the path the gas takes is determined by the global circulation pattern at the time of release (Viscardy et al., 2016). Simulations show that it can then take several weeks for it to become uniformly mixed, as such, the detection of vertical layers of methane can be indicative of a recent emission.

GEM-Mars uses a turbulent parameterization scheme to provide eddy diffusion coefficients, which are then used in calculating vertical transport of constituents in the atmosphere. This scheme uses mixing lengths to estimate the turbulent diffusivity, which is then used to calculate the eddy diffusion coefficients, K(z). The turbulent diffusivity is related to the velocity scale and length scale of turbulent eddies, which are estimated using empirical relationships based on variables in the model including wind speed, temperature, atmospheric stability and surface roughness (in our case, over Gale Crater). Eddy diffusivities are used to calculate turbulent mixing and are based on local gradients of wind and potential temperature (Holtslag & Boville, 1993).

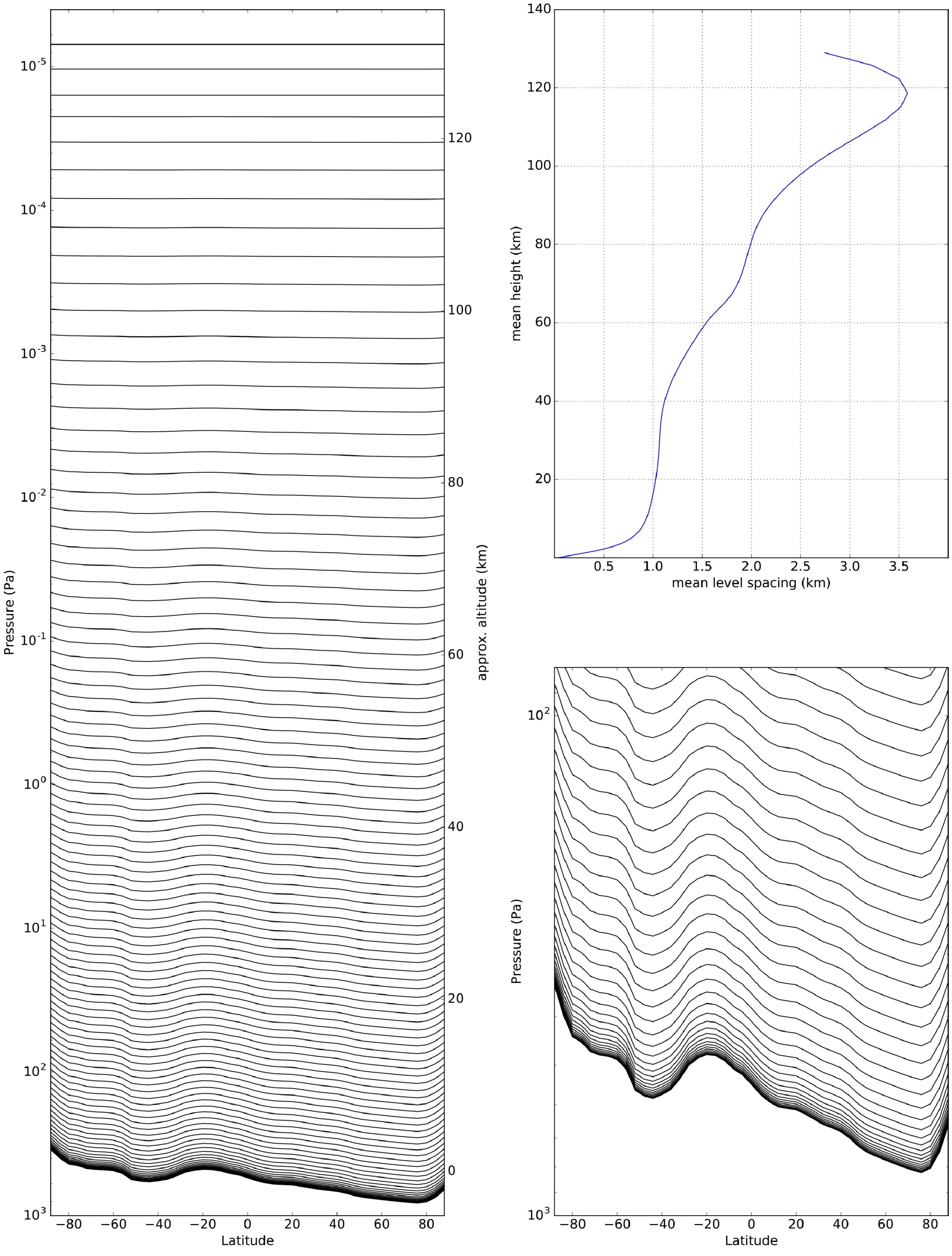

Figure 2.1: GEM-Mars vertical profile. (left) 103 thermodynamic levels, (top right) mean spacing between each thermodynamic level, (bottom right) close-up of near-surface levels. Momentum levels lie exactly halfway between each thermodynamic level (Neary & Daerden, 2018).

Several parameters are used to calculate the diffusivities, which involve the transport and mixing of atmospheric constituents by convective turbulence, and are discussed in the subsequent sections.

Turbulent transport in the surface layer is based on the Monin-Obhukov similarity theory (Jacobson, 2005, Section 8.4.2), in which variables are scaled by a characteristic value and become dimensionless. These variables are then used to relate eddy diffusion coefficients to surface fluxes and atmospheric stability in the surface layer. When dust absorbs solar radiation, or when strong wind shear creates regions of convective instability in the model, temperature, momentum, and constituents are vertically mixed over the unstable layers in the model, regaining neutrality. To compute the diffusion coefficients at the surface layer, we first compute the bulk Richardson number (Ri_b), which is used to determine the stability of the surface layer:

$$Ri_b = \frac{g((\overline{\theta}_v(z_r) - \overline{\theta}_v(z_{0,h}))(z_r - z_{0,m})^2}{\overline{\theta}_v(z_{0,h})(\overline{u}(z_r)^2 + \overline{v}(z_r)^2(z_r - z_{0,h})} \tag{2.2}$$

Where g is the acceleration due to gravity (3.721 m s^{-2}), z is height above the surface, $\overline{\theta}_v(z_{0,h})$ is the virtual potential temperature, $\overline{u}$ is horizontal wind speed. Using the bulk Richardson number, the friction velocity (u_*), and potential temperature (θ_*) are determined from Jacobson (2005) (eq 8.40, 8.41), calculated as

$$u_* \approx \frac{k|\overline{v}_h(z_r)|}{\ln(z_r/z_{0,m})}\sqrt{G_m} \tag{2.3}$$

and

$$\theta_* \approx \frac{k^2|\overline{v}_h(z_r)|[\overline{\theta}_v(z_r) - \overline{\theta}_v(z_{0,h})]}{u_* Pr_t \ln^2(z_r/z_{0,m})} G_h \tag{2.4}$$

where

$$G_m = 1 - \frac{9.4 Ri_b}{1 + \frac{70k^2(|Ri_b| z_r / z_{0,m})^{0.5}}{\ln^2(z_r / z_{0,m})}}, Ri_b \leq 0 \tag{2.5}$$

$$G_h = 1 - \frac{9.4 Ri_b}{1 + \frac{50k^2(|Ri_b| z_r / z_{0,m})^{0.5}}{\ln^2(z_r / z_{0,m})}}, Ri_b \leq 0 \tag{2.6}$$

$$G_m, G_h = \frac{1}{(1 + 4.7 Ri_b)^2}, Ri_b > 0 \tag{2.7}$$

$Pr_t = 0.95$ is the turbulent Prandtl number, which approximates the ratio of the diffusion coefficient for momentum to that for energy, and describes how efficiently heat is transferred. A higher Prandtl number (> 1) means the medium is less conductive to heat. Friction velocity is physically linked to the transport of momentum between levels within the PBL, and the potential temperature is used to define stability. Unstable stratification enhances vertical turbulent mixing, occurring when an air parcel becomes less dense than the surrounding air as it ascends. Solar heating is a common driver of instability in the PBL, where buoyant forces cause surface-heated air to rise and mix with higher layers. In this context, potential temperature serves as a defining factor for such conditions. Specifically, when the potential temperature decreases with height, the temperature profile is deemed unstable since the potential temperature remains constant during an adiabatic pressure change of an air parcel.

Based on u_* and θ_*, we can determine the Monin-Obukhov length (L):

$$L = \frac{u_* \overline{\theta}_v}{k g \theta_*} \tag{2.8}$$

Where k is the von Karman constant, which is set to 0.4 and relates the velocity profile in the atmosphere to the surface roughness length. L is then used to recalculate u_* and along with θ_*, is used to calculate the diffusion coefficients at the surface depending on the stability conditions. L is a length scale (m) proportional to the height above the surface at which turbulence from buoyancy first dominates turbulence from shear (Jacobson, 2005). When L is small and negative, there is a large instability due to buoyancy with increasing height. Conversely, positive values of L with increasing height correspond to stable stratification.

From Holtslag and Boville (1993), convective transport above the surface layer is parameterized using K-theory, where the vertical turbulent flux of a quantity is taken proportional to the local gradient of the transported quantity, and depends on factors such as surface roughness, stability, and stratification. This is defined by:

$$\overline{\omega' C'} = -K_c \frac{\partial C}{\partial z} \tag{2.9}$$

C is an element of specific humidity, potential temperature, zonal wind, and meridional wind. K_c is the eddy diffusivity for C, and is usually taken as a function of a length scale l_c, and local vertical gradients of wind and potential temperature:

$$K_c = {l_c}^2 S F_c(Ri) \tag{2.10}$$

Where S is the local shear given by:

$$S = |\frac{\partial V}{\partial z}| \tag{2.11}$$

Where V is the horizontal velocity vector. l_c is then given by:

$$\frac{1}{l_c} = \frac{1}{kz} + \frac{1}{\lambda_c} \tag{2.12}$$

Where k is the von Karman constant and λ is the asymptotic length scale, in which turbulence becomes nearly the same in all directions. Vertical turbulent fluxes are computed depending on the stability of the surface layer which depends on θ_*. If $\theta_* > 0$, it is stably stratified, and K-theory is used. For this, the bulk Richardson number is computed as the gradient Richardson number, and the mixing length in each vertical layer is computed, from which the diffusion coefficients are computed. The gradient Richardson number (Ri_g) is used to identify the overall stability of the atmospheric boundary layer and quantifies the ratio of buoyancy to mechanical shear. The gradient Richardson number is defined as:

$$Ri_g = \frac{\frac{g}{\overline{\theta}_v}\frac{\partial\overline{\theta}_v}{\partial z}}{(\frac{\partial u}{\partial z})^2 + (\frac{\partial v}{\partial z})^2} \tag{2.13}$$

$\frac{\partial\overline{\theta}_v}{\partial z}$ is the change in potential temperature with height, and (u, v) are the east and north wind components. Low Ri values suggest a higher vertical shear relative to buoyancy, where high Ri values suggest a higher buoyancy relative to mechanical shear. The bulk and gradient Richardson numbers are used for determining the ratio of turbulence due to buoyancy compared to that from shear. When $Ri < 0$, the potential virtual temperature is decreasing with altitude and the atmosphere is buoyantly unstable and turbulent. When $Ri > 0$, the atmosphere is buoyantly stable and no free convection turbulence occurs. When a large and positive Ri decreases to less than the critical Richardson number (Rc) of 0.25, laminar flow turns to turbulent flow and wind shear increases. Above the termination Richardson number (Ri_T) of 1.0, turbulent flow is laminar (Table 2.1).

Above the PBL, vertical mixing is simulated with a parameterization of eddy diffusion (Holtslag & Boville, 1993; Savijärvi, 1995), in which the eddy diffusion coefficients were calculated using a mixing length and stability function derived from the gradient flux Richardson number. Near the surface, turbulence and mixing length

Table 2.1: Characteristics of the vertical flow of air depending on the values of Ri_b and Ri_g, from Jacobson (2005)

Ri_b or Ri_g	Type of flow	Level of turbulence due to buoyancy	Level of turbulence due to shear
Large, negative	Turbulent	Large	Small
Small, negative	Turbulent	Small	Large
Small, positive	Turbulent	None (weakly stable)	Large
Large, positive	Laminar	None (strongly stable)	Small

are limited by the ground, and in the free atmosphere, turbulence is limited by a maximum mixing length. The stability function was chosen from (Haberle et al., 2001), and the mixing length was set to 500 m. For this case ($Ri < 0$):

$$f(Ri) = (1 - 64Ri)^{0.5} \tag{2.14}$$

In the stable case, we use the stability function as given by Savijärvi (1995) (when $Ri > 0$):

$$f(Ri) = max(0.05, 1 - 5Ri) \tag{2.15}$$

Depending on the stability, we compute the diffusion coefficients:

$$K = \lambda^2 \sqrt{\frac{\Delta \overline{u}}{\Delta z}^2 + \frac{\Delta \overline{v}}{\Delta z}^2} f(Ri) \tag{2.16}$$

GEM-Mars uses the Monin-Obhukov similarity theory to compute turbulent transport in the surface layer. Ri_b is computed and used to determine the stability of the surface layer. Depending on the case, the terms used in the similarity theory are calculated, which include the dimensionless wind shear, dimensionless potential temperature gradient, and the Monin-Obhukov length. From these terms, the stability is defined and the diffusion coefficients at the surface can be computed. Above the surface layer, the potential temperature is used to determine the stability, then the gradient Richardson number and mixing length in each layer with increasing height are computed and from these, the diffusion coefficients are computed. Above the PBL, the stability functions use a fixed free-atmosphere mixing length of 500 m.

Parameters such as the Monin-Obukhov length, potential temperature scale, and friction wind speed can be determined using the roughness length (here it is that of Gale Crater and equal to 0.324 m). GEM-Mars utilizes these parameterizations to describe turbulent vertical transport in the Martian atmosphere. Using the eddy diffusion coefficients produced by GEM-Mars, we are able to more accurately characterize how emissions of methane would behave in the PBL.

2.1.3 Combining Model Techniques for Mixing Ratio Outputs

The outputs provided by GEM-Mars are constrained to a $4^{\circ} \times 4^{\circ}$ grid containing Gale Crater and include surface temperature, diffusion coefficients, model heights and pressures (Fig. 2.2). Each output parameter is given in time steps of $1/48^{th}$ of a sol, with 48 timesteps in total.

Output variables for 35 different solar longitudes were provided from L_s=0° to L_s=350°, with intervals of 10 L_s. Then, ten of the closest equivalent solar longitudes where SAM-TLS took measurements were selected (L_s=10°, 30°, 70°, 100°, 140°, 160°, 220°, 270°, 300°, 330°), with heights interpolated to 3 km, with each level thickness equal to 1 m. These output parameters were then used in the VDM to output the methane mixing ratio based on a provided surface flux in ppbv min^{-1}. The approach used to determine the fluxes that produced mixing ratios closely aligned with the

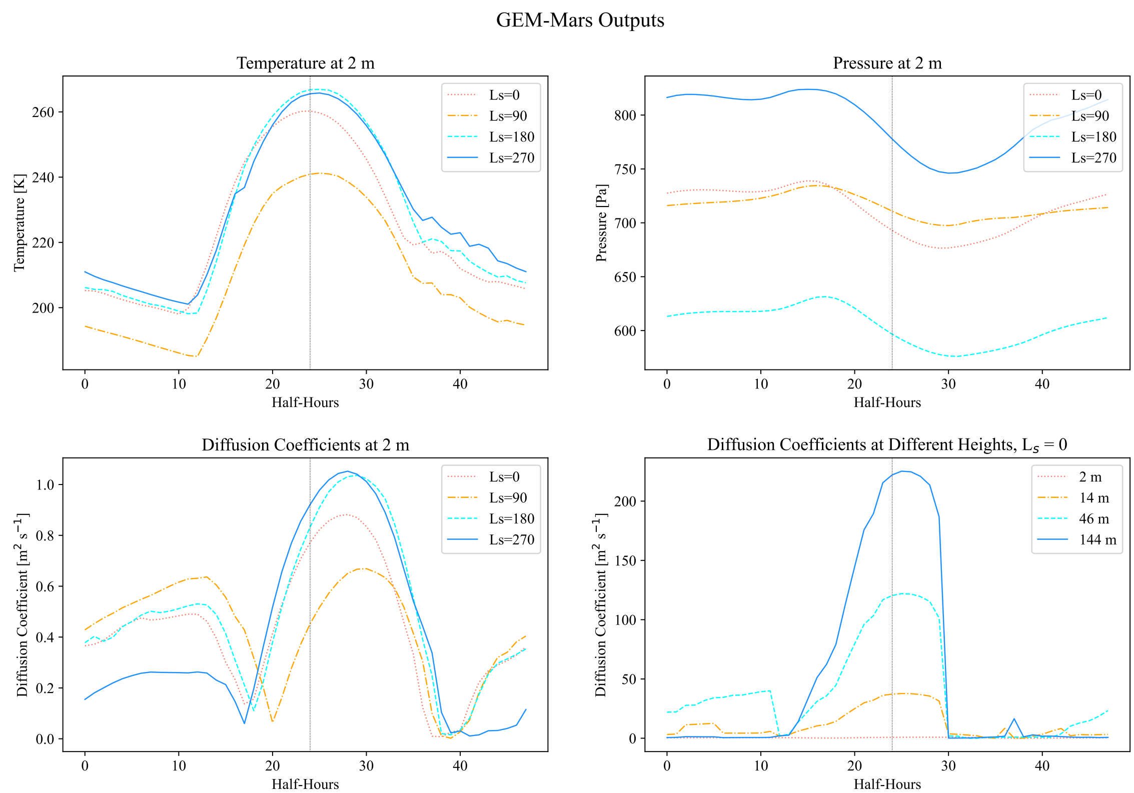

Figure 2.2: GEM-Mars outputs through one sol. (top left) Temperatures at 2 m for $L_s = 0°, 90°, 180°, 270°$. (top right) Pressure at 2 m for $L_s = 0°, 90°, 180°, 270°$. (bottom left) Diffusion coefficients at 2m for $L_s = 0°, 90°, 180°, 270°$. (bottom right) Diffusion coefficients at heights of 2 m, 14 m, 46 m, and 144 m, which are the bottom four model levels. The vertical black line signifies noon (12:00).

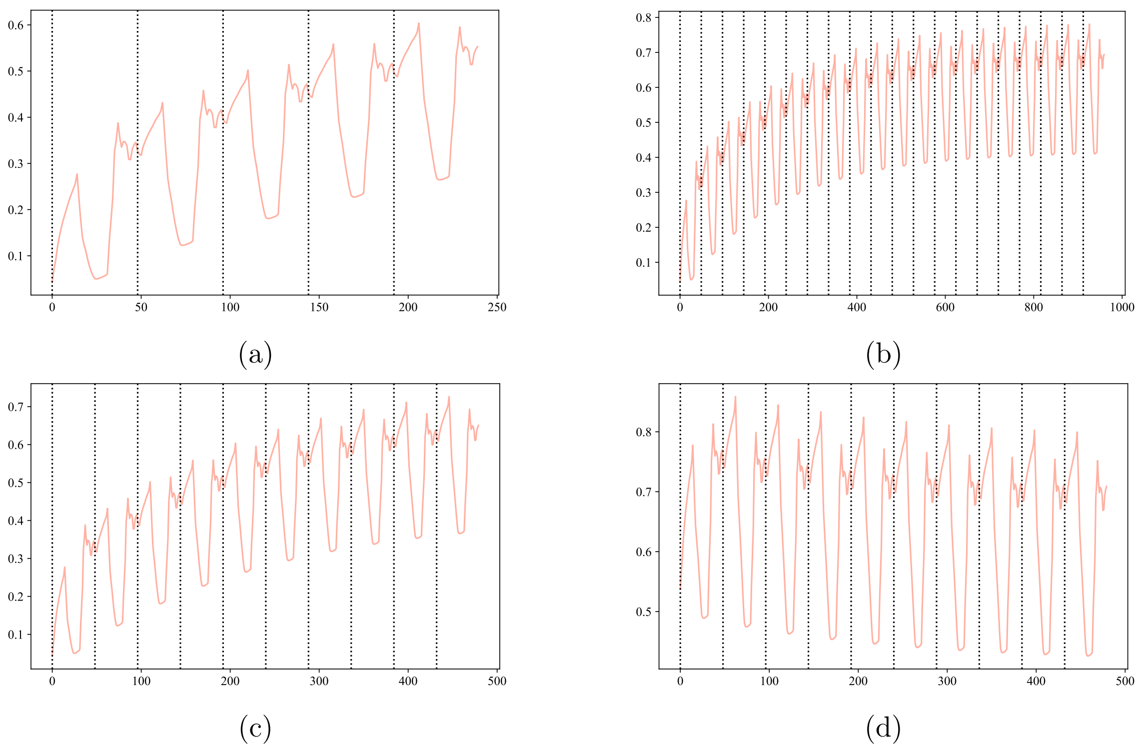

Figure 2.3: Model spin-up comparisons for $L_s = 160°$. (a) 5 day spin-up with background mixing ratio set to 0 ppbv. (b) 20 day spin-up with background mixing ratio set to 0 ppbv. (c) 10 day spin-up with background mixing ratio set to 0 ppbv. (d) 10 day spin-up with background mixing ratio set to 0.5 ppbv. A longer spin-up time paired with a background mixing ratio that is close to the SAM-TLS mixing ratio for the same date and time gets closer to equilibrium.

SAM-TLS measurements involved adjusting the values iteratively until an accurate match was achieved. An initial estimation was made based on the fluxes calculated by Moores et al. (2019b), and was then adjusted to best match the SAM-TLS values until the error was within 0.001 ppbv.

The model was allowed to run for ~ 20 repetitions or until an equilibrium was met, which varied based on the background mixing ratio set relative to the desired abundance (Fig. 2.3). The flux was then converted to units of kg m^{-2} sol^{-1} using the provided mean surface temperature and density for the time and L_s which correlated to the time and L_s the corresponding SAM-TLS measurement took place.

To convert from ppbv min^{-1} to kg m^{-2} sol^{-1}, we first find density (ρ) by taking the mean temperature of the bottom layer:

$$\rho = \frac{MP}{RT} \tag{2.17}$$

Where M = 0.044 is the molecular mass of CO_2 in kg mol^{-1}, P is the surface pressure in Pa, R = 8.314 is the gas constant in J mol^{-1}, and T is the surface temperature in K.

From this, we calculate the flux:

$$F = \phi \frac{r \rho t}{10^9} \tag{2.18}$$

Where F is the flux in kg m^{-2} sol^{-1}, ϕ is the flux in ppbv min^{-1}, r = 0.37 is the molar mass ratio of methane to CO_2, and t = 1479 is the minutes in a sol. From this, we were able to calculate the corresponding fluxes that reproduced each SAM-TLS measurement, as well as use the input parameters to plot the diurnal variation of methane at various heights given a constant surface seepage.

2.2 Results

2.2.1 Methane Vertical Diurnal Behaviour

Figure 2.4 and 2.5 show the modeled diurnal behavior of the diffusion coefficients within the PBL compared with the methane mixing ratio for the same duration and heights. Each plot begins at local midnight and corresponds to six of the ten solar longitudes where SAM-TLS has made measurements which best match the input solar longitudes (L_s = 10°, 30°, 70°, 100°, 140°, 160°, 220°, 270°, 300°, 330°). Mixing ratio plots are generated using the diffusion coefficients provided by GEM-Mars, and both are significantly impacted by the time of day and height above the surface.

The diffusivity increases as the surface temperature increases at sunrise ($\sim$ 05:00-07:00), reaching a peak slightly after noon of around 1000 m^2 s^{-1} at heights of up to 3 km, highlighting the PBL depth. At approximately 16:00 during each solar longitude, a sharp decrease in diffusivity is seen at all heights, then again at approximately $\sim$ 20:00 when the diffusivity drops down to minimum levels closer to the surface. At this time, during sunset, the PBL collapses down to around 90 m, characterized by low diffusivity on the order of 0.1 m^2 s^{-1}. Through the night, the surface temperature becomes colder than the air above due to radiative cooling, and turbulent mixing becomes inhibited. At this time, the diffusion coefficients stay relatively low, and decrease to lower values above the PBL.

Compared to the diffusivity, the overall behavior of the methane mixing ratio shows a build-up overnight, reaching heights of approximately 100 m until sunrise, when the methane begins to diffuse within the PBL more rapidly. At sunset, when the diffusion decreases rapidly, the methane once again is able to build up to higher amounts, rapidly at first, reaching heights of approximately 50 m - 90 m,then experiences a slower build-up in the subsequent timesteps. During each solar longitude, while methane does build up over night, the maximum values are seen at approximately 20:00, when the diffusion coefficients are at a minimum.

As solar longitude changes, the amount of surface heating changes, varying the diurnal diffusivity during different seasons. The corresponding mixing ratio plots show a strong dependence on the diffusion coefficients; larger diffusion coefficients corresponds to low mixing ratios. During aphelion cloud belt (ACB) season (L_s= 45°- 160°), the presence of clouds can affect the amount of solar radiation reaching the surface, which decreases turbulent mixing in the atmosphere (Benson et al., 2003; Cooper et al., 2021). As a consequence, after a sharp decrease in diffusivity, the diffusion coefficients for L_s= 70°, 100°, and 160° rise back to a steady amount near midnight with minimal mixing after sunset (Fig 2.4a,c,e). Figure 2.4b,d,f shows the methane abundance for the same days, where two individual spikes of higher abundances are seen at around 18:00 and 20:00, corresponding to the low values of diffusivity, which allows the methane to build up to higher values.

During the dust storm season (which typically begins at L_s= 180°- 225° and ends around L_s= 315°- 360°), the atmosphere is impacted by widespread dust storms that can lead to increased shear from dust particles and other constituents. During this time, circulation at Gale Crater is likely to be disrupted by wind shear, causing more variations in diffusivity. These variations are typically seen towards the top of the mixing layer where the methane concentration is less impacted.

Similar to L_s= 70°, 100°, and 160°, for L_s= 220°, 300°, and 330°, diffusion in the evening, from about 22:00 to 07:00, remains at a steady amount of $\sim 200\ \mathrm{m^2\ s^{-1}}$ near ~ 100 m in altitude (Fig. 2.5a,c,e). As a consequence, the methane mixing ratios at these heights and times are decreased, but not zero as methane can still build up in low amounts over night. However, more variation in the diffusion coefficients are seen near sunset for these solar longitudes, where spikes of higher values occur higher up,

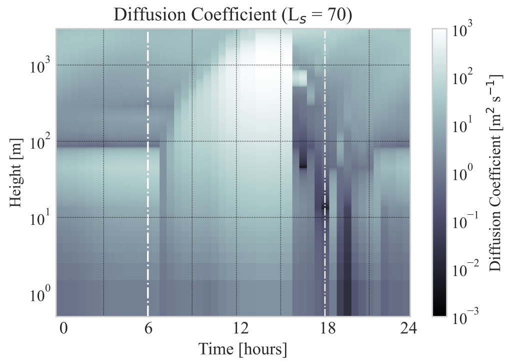

(a) $L_s = 70°$

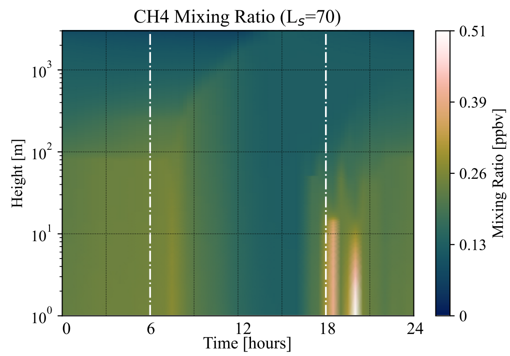

(b) $L_s = 70°$

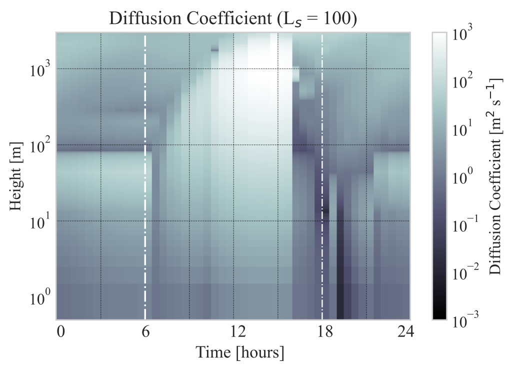

(c) $L_s = 100°$

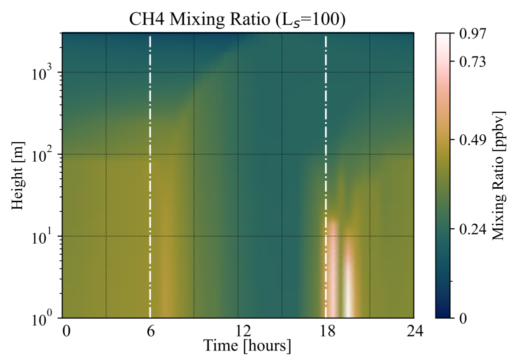

(d) $L_s = 100°$

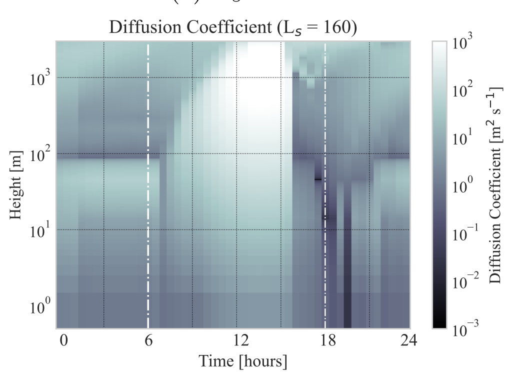

(e) $L_s = 160°$

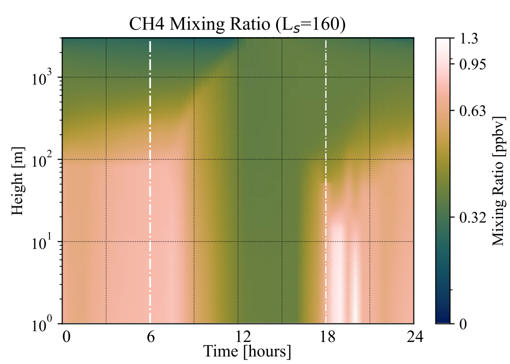

(f) $L_s = 160°$

Figure 2.4: Diurnal diffusion coefficients up to heights of 3 km, and the corresponding methane mixing ratios through one sol during $L_s = 70°$, 100°, and 160° during ACB season, where near-surface mixing is decreased. The white vertical lines at 06:00 and 18:00 represent sunrise and sunset, respectively.

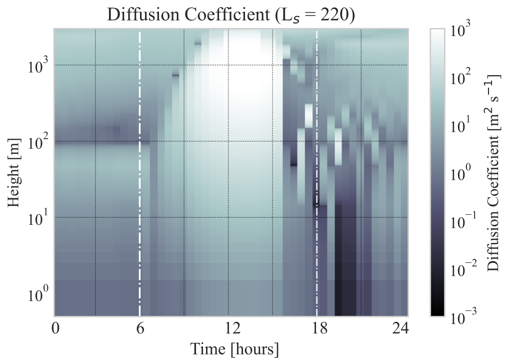

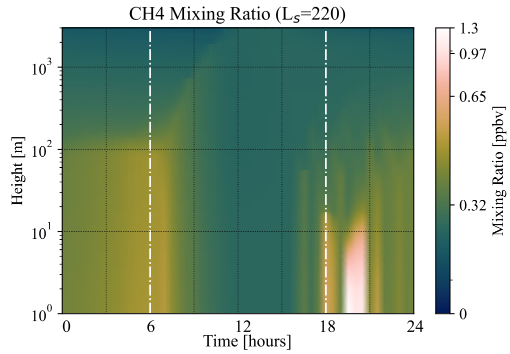

(a) $L_s = 220°$

(b) $L_s = 220°$

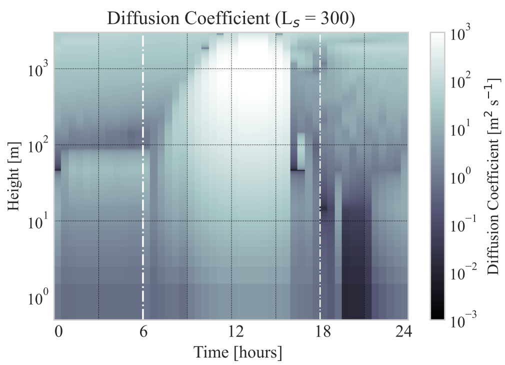

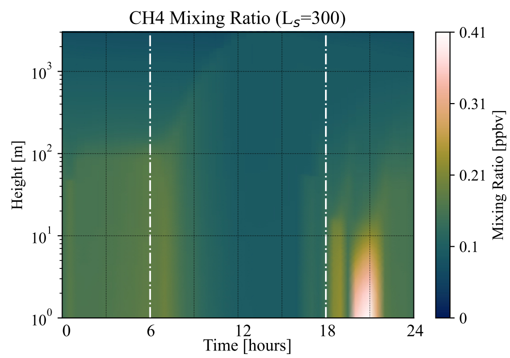

(c) $L_s = 300°$

(d) $L_s = 300°$

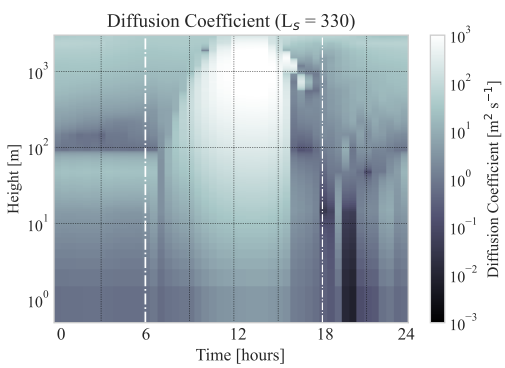

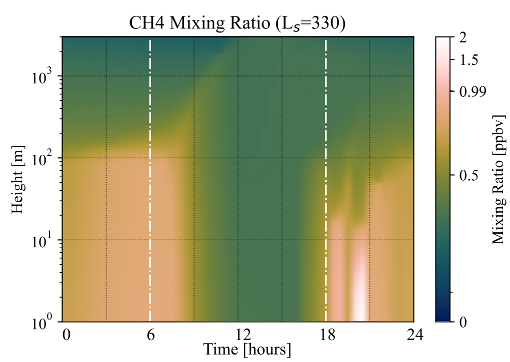

(e) $L_s = 330°$

(f) $L_s = 330°$

Figure 2.5: Diurnal diffusion coefficients up to heights of 3 km, and the corresponding methane mixing ratios through one sol during $L_s = 220°$, 300°, and 330°. This time period represents the dust storm season Mars, where mixing is increased within the PBL, leading to more variations in diffusion coefficients within the PBL during and following sunset. The white vertical lines at 06:00 and 18:00 represent sunrise and sunset, respectively.

at around 100 m.

Closer to the surface (< 10 m), the mixing is less variable, with a similar increase in diffusivity at approximately 19:00 and subsequent decrease at approximately 20:00. Again, we see methane building up at these times as a consequence of the low values of the diffusion coefficients. During each solar longitude, these high values of methane mixing ratios are seen at approximately 18:00, and then again near 20:00, corresponding to low diffusion coefficients. Methane again builds up over night until sunrise, when diffusivity levels increase again, and methane is mixed more vigorously.

Figure 2.6a,b shows how the diurnal change in methane mixing ratio varies with different heights during $L_s = 70°$ and $160°$, which are chosen as an example to be consistent with the season during which SAM-TLS measured the minimum and maximum methane abundances. During both solar longitudes, the mixing ratio at all heights experiences a brief increase at sunrise, beginning with the lowest heights. As the methane is diffused vertically, the mixing ratio at each subsequent height then decreases. At heights closer to the surface, the mixing ratio decreases down to lower than the nighttime abundances. Through the night starting at local midnight, the methane mixing ratio builds, starting near sunset up through sunrise of the following sol. As the sun rises at $\sim$ 06:00, and the diffusivity levels increase, the methane mixing ratio at heights close to the surface decreases, followed by a decrease in the mixing ratios at the subsequent heights above the surface. As the methane mixes in the PBL, the mixing ratio at higher altitudes start to decrease as well, all reaching a minimum at approximately local noon. During $L_s = 160°$, this pattern occurs in a similar way, though the overall abundances are higher and there is more variation in the lower level values after sunset.

Before sunrise, the diffusion coefficients near the surface, at a height of approximately 20 m, are higher than those at 20 m and 100 m. However, these diffusion

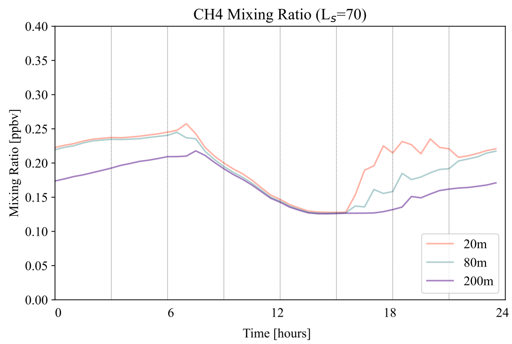

(a) $L_s = 70°$

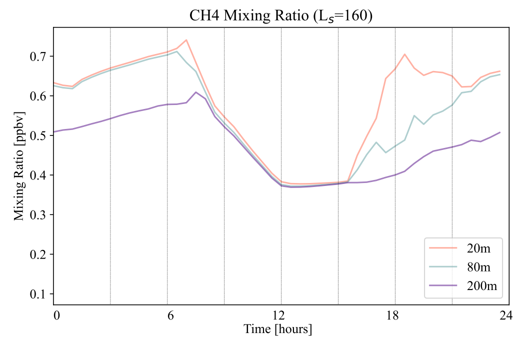

(b) $L_s = 160°$

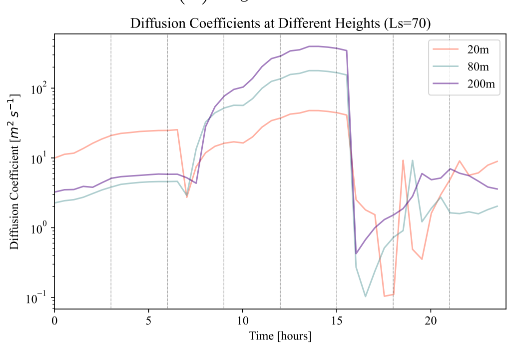

(c) $L_s = 70°$

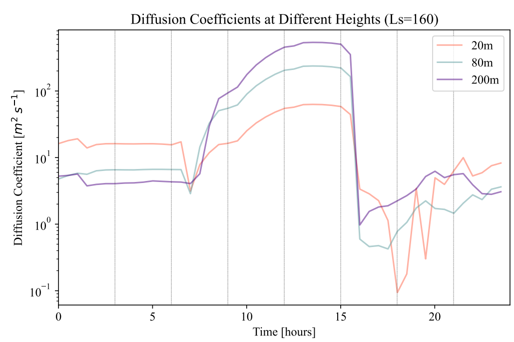

(d) $L_s = 160°$

Figure 2.6: Methane mixing ratio values and diffusion coefficients at different heights. (a) $L_s = 70°$ is chosen as a time of minimum methane abundance. The mixing ratio decreases starting at around sunrise, then rises again near sunset, with higher values closer to the surface. (b) $L_s = 160°$ is chosen as a time of maximum methane abundance. Compared to $L_s = 70°$, the methane mixing ratio is larger at each height and experiences more variation in values after sunset. (c, d) All values of diffusion coefficients at each height increase through the day then begin to decrease at sunset, though more variation is seen after sunset with lower heights.

coefficients near the surface are lower than those at the higher altitudes. Throughout the day, as the PBL grows, the diffusion coefficients at 20 m stay lower that those at 80 m and 200 m (Fig. 2.6c,d). The variations after sunset can also be clearly seen at lower levels before smoothing back out near midnight.

2.2.2 Flux Calculation and Comparison to Moores et al. (2019)

For each measurement recorded by SAM-TLS, Table 2.2e depicts the fluxes needed to reproduce the corresponding concentration at the time the measurement was taken. Again, we focus on ten solar longitudes which are closest to when SAM-TLS made methane measurements. By adjusting the initial surface flux, we matched the modeled methane concentration to that of SAM-TLS at the time, height, location, and solar longitude that each measurement was taken. This allowed for the determination of the necessary surface fluxes needed to reproduce the measured concentration values at the time they were taken, given the diffusion coefficients and temperatures output by GEM-Mars.

This work was done in order to compare our values to the methane flux calculated by Moores et al. (2019b), which describes a diurnal microseepage process to account for the SAM-TLS concentrations using TGO-ACS/NOMAD constraints. The fluxes calculated by Moores et al. (2019b) are found using column masses from boundary layer height estimations, assuming a temperature of 180 K, a pressure of 800 Pa, and a diffusion timescale of $\Delta t = 12$ hours.

Using this technique, it was found that the fluxes are consistent with a microseepage of 1.5 x 10^{-10} kg m^{-2} sol^{-1} at depth. All predicted values are also much smaller than those suggested by Korablev et al. (2019), who assumed daytime diffusivities. It can be seen in Table 2.2 that the fluxes found by Moores et al. (2019b) are within approximately one order of magnitude to those derived by modeling techniques.

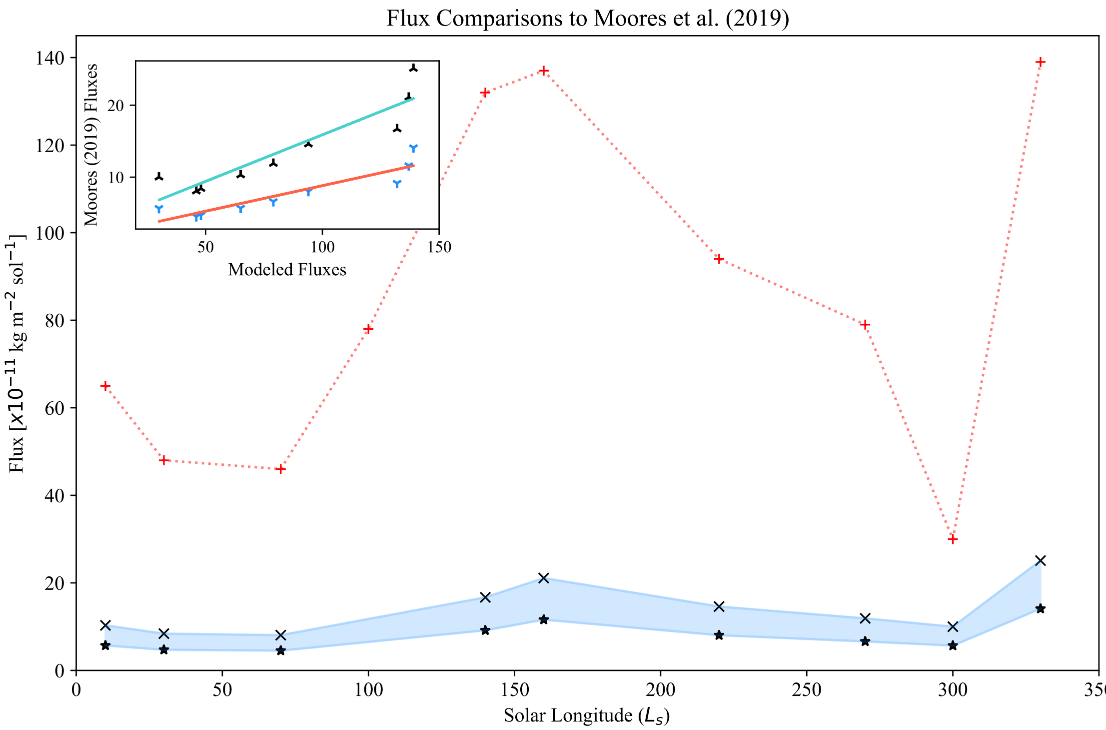

Figure 2.7: Fluxes calculated in this work (red plus signs) versus fluxes calculated by Moores et al. (2019b) (black stars represent fluxes assuming stable stratification, black Xs represent fluxes assuming the near-surface layer to be well mixed). A similar trend is shown, though the fluxes presented in this work are approximately one order of magnitude larger that those calculated by Moores et al. (2019b). The quality of the fit between this work and the work presented by Moores et al. (2019b) is described by the inset plot: the black markers are the Moores et al. (2019b) flux values assuming the near-surface layer to be well mixed, and the blue markers are the flux values assuming stable stratification. The quality of the fit is represented as a least-squares fit of this work to that of Moores et al. (2019b) for each condition (light blue and red lines).

Table 2.2: Methane fluxes needed to reproduce SAM-TLS observations

Sol[a]	Time[b]	L_s from Webster et al. (2018)	L_s from GEM-Mars	Flux from Moores et al. 2019 (x 10^{-11} kg m^{-2} sol^{-1})	Model predicted flux (x 10^{-11} kg m^{-2} sol^{-1})	SAM-TLS Abundance (ppbv)
1709	00:00	10.84	10	5.7-10.3	65	0.319
1086.06	01:30	32.81	30	4.72-8.41	48.04	0.241
1169.02	00:30	70.57	70	4.52-8.06	46	0.235
573.08	01:57	103.48	100	N/A	78	0.419
1322	00:00	142.46	140	9.16-16.7	132	0.502
684.06	01:30	158.61	160	11.6-21.1	137	0.653
1451.06	01:30	216.58	220	8.04-14.6	94	0.5
1527.06	00:30	265.78	270	6.62-11.9	79.7	0.357
1579.00	00:00	298.76	300	5.67-10	30	0.246
965.99	23:45	331.57	330	14.1-25.1	139	0.609

(a) Sols from Webster et al. (2018). Decimal portion of the sol represents local time such that, for instance, sol 1169.02 represents local time 00:30; (b) Local time corresponding to the decimal portions in (a).

However, the higher values calculated in this work are not unexpected considering the higher values of diffusivity provided by the GEM-Mars outputs. These values require higher fluxes in order to match the same mixing ratio as compared to the diffusivity values used in Moores et al. (2019b). Though our fluxes are approximately one order of magnitude larger than those calculated by Moores et al. (2019b), a similar trend can be seen, as highlighted in Fig. 2.7. In both works, higher flux values are a consequence of larger methane mixing ratios; the highest fluxes seen during $L_s = 160°$ and $330°$, coinciding with when the SAM-TLS measurements also report maximum methane abundances.

2.3 Discussion

2.3.1 Diffusivity Variation After Sunset

During $L_s = 220°$, distinct variations in the diffusion coefficient values at specific heights can be seen near sunset, from approximately 16:00 to 21:00. As mentioned in section 2.1.2, after sunset, $\theta_* > 0$, and thus the atmosphere is in the stable regime. At this time, the height of the PBL correlates with the first point from the surface up where the gradient Richardson number is greater than 0.5 (below which the air is dynamically unstable), and is calculated via equation 2.13. As such, the values of the diffusion coefficients after sunset depend on the shear and gradient Richardson number. Any variations are most likely caused by specific atmospheric processes, such as the presence of inversion layers, the impact of local or regional weather, or the influence of aerosols or wind shear.

One possible explanation for the variations in the mixing ratio after sunset is increased dust storms, which can influence atmospheric shear. Figure 2.8 shows the dust opacity modeled by GEM-Mars, which begins to increase at approximately $L_s = 170° - 180°$ during dusty season. When dust is heated by solar radiation or wind shear and creates regions of instability in GEM-Mars, temperature, momentum, and constituents mix vertically over the unstable layers to regain stability. Dust storms can create strong and variable turbulent eddies, leading to increased diffusion in the PBL, and variations in the diffusion coefficients. The methane mixing ratio during these solar longitudes are slightly impacted, though at heights greater than $\sim$ 100 m, where these variations occur, the methane is mostly diffused down to minimal values.

Additional output parameters from GEM-Mars can also provide additional details on the diurnal behaviour of methane. The friction velocity and wind speeds provide context to the drop in diffusivity near sunset. As the surface layer becomes cooler

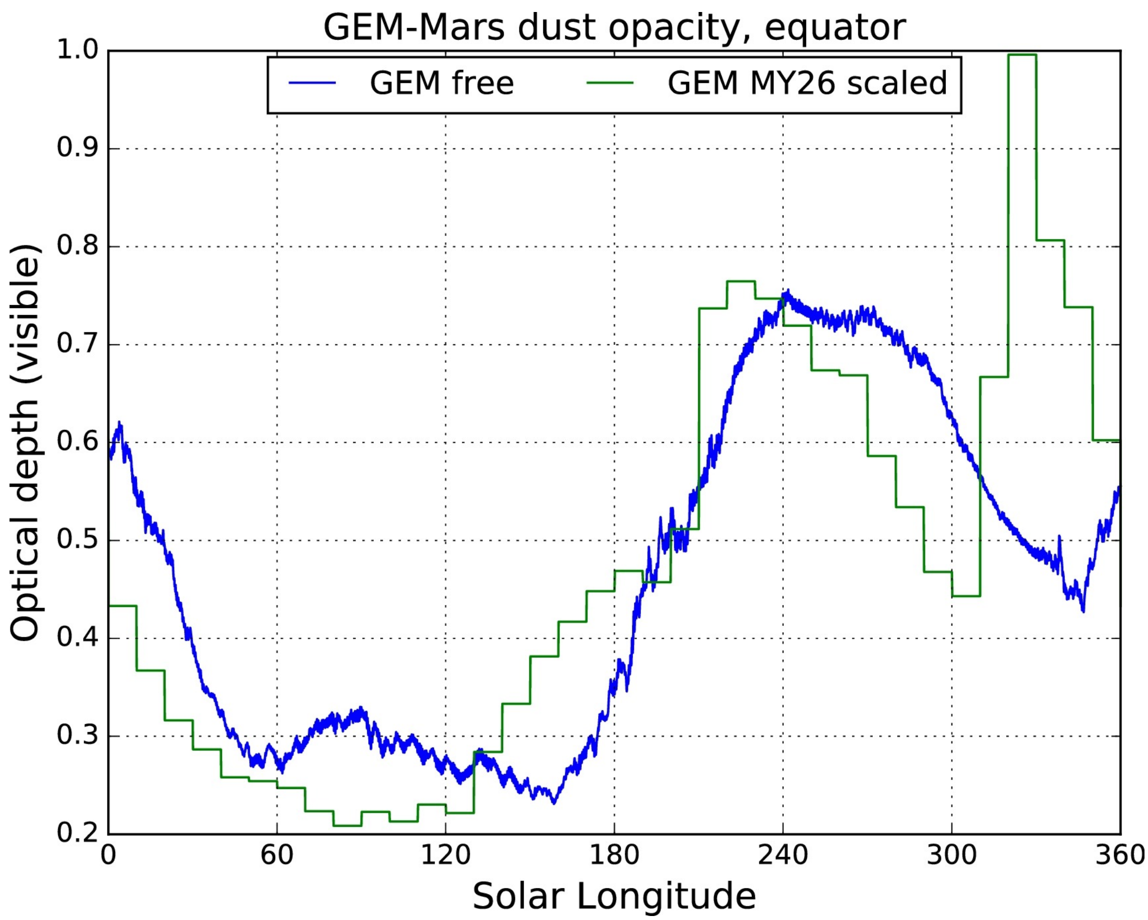

Figure 2.8: From Neary and Daerden (2018) (Eq. 5). Equatorial zonal mean dust opacity. The blue line is the dust optical depth for the free-running dust lifting scheme, compared with the optical depths scaled to MY26 climatology (green). Dust increases during $L_s = 170°$ - $180°$ and begins to decrease again at around $L_s = 270°$ - $280°$. During this time, the diffusion coefficients may be impacted by dust being heated by solar radiation or wind shear.

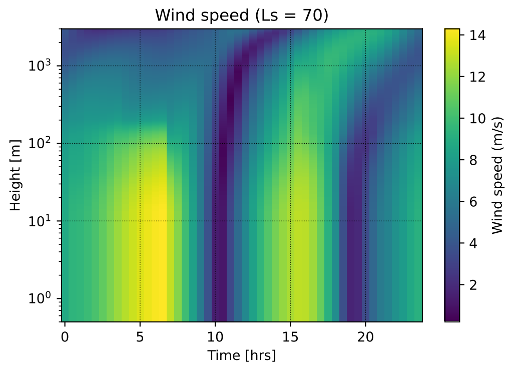

(a) L$_s$ = 70°

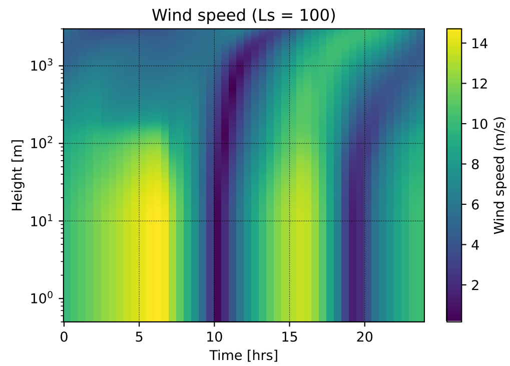

(b) L$_s$ = 100°

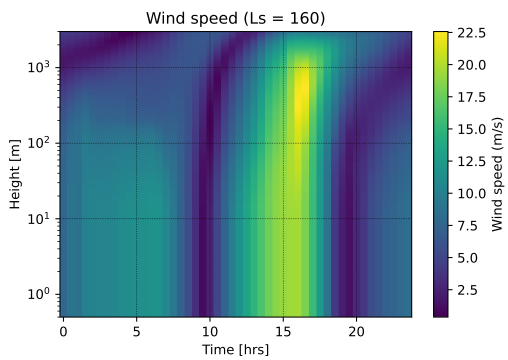

(c) L$_s$ = 160°

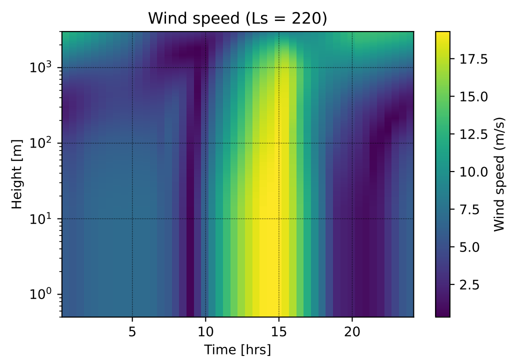

(d) L$_s$ = 220°

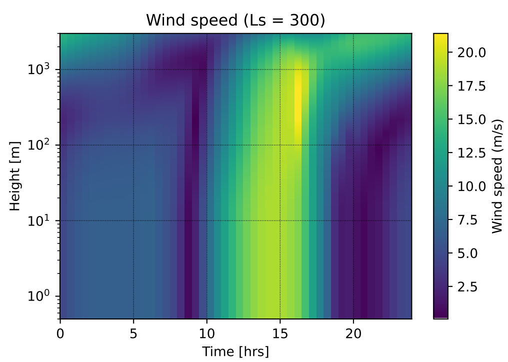

(e) L$_s$ = 300°

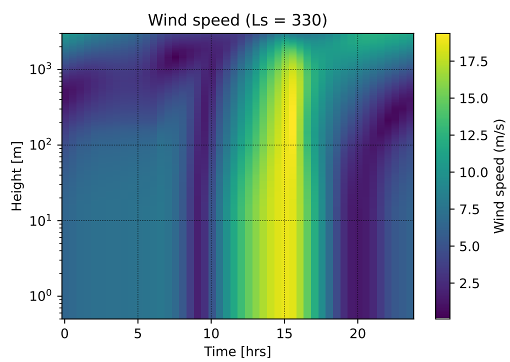

(f) L$_s$ = 330°

Figure 2.9: GEM-Mars wind speeds. Wind speeds decrease near 07:00 and 18:00, and build up to a maximum near 15:00, and at 05:00 for $L_s = 70°$ and 100°. The decrease in wind speeds near 18:00 align with the decrease in diffusivity seen at approximately the same time of day, leading to an increase in the methane mixing ratio.

than the air above it, friction causes near-surface wind speeds to decrease. Meanwhile, winds at higher altitudes are more isolated from surface energy dissipation and remain faster. Because of this difference in wind speeds from a temperature inversion, the diffusivity experiences a rapid decrease, resulting in a higher accumulation of methane. Combining zonal and meridional wind gives the total wind speed, shown in Fig. 2.9.

In Fig. 2.9, we can see a drop in wind speeds near 18:00, at the same time of day we previously saw an increase in the methane mixing ratio. We also see higher shear in the lowest layers through the night which is more prominent in the first half of the year (L_s = 70°-100°), with values reaching up to $\sim$ 14.7 m s^{-1} near sunrise during L_s = 100°. This is comparable to the results of wind speeds found with GEM-Mars in a multi-model inter-comparison for Jezero crater, where GEM-Mars values were found to be higher through the night (Fig. 2.10e) (Newman et al., 2020).

The diffusivity levels can also be compared to the friction velocity (u_*), where $u_* = \sqrt{\tau/\rho_a}$, τ is the wind shear stress, and ρ_a is the air density. The turbulent friction that the rough surface of the planet exerts on the air causes vertical wind shear, which produces eddies. The greater the height of the roughness elements on the surface, and the greater the horizontal wind speed, the greater the shear. As such, the friction velocity is the measure of the vertical flux of horizontal momentum at the surface. As the friction velocity increases, the mechanical turbulence increases, and the constituents mix faster. Figure 2.11 shows that combining the u_* values for each solar longitude reveals a fast decrease near sunset, similar to wind speeds. This change in wind speed and u_* may be affecting the diffusion coefficients such that they decrease rapidly at sunset, causing a moment of very low mixing.

The sharp decrease in diffusion coefficients and the subsequent spikes of higher values after sunset may also be due to the decrease in wind shear, which relates to the gradient Richardson number. Near sunset, the lower atmospheric layers

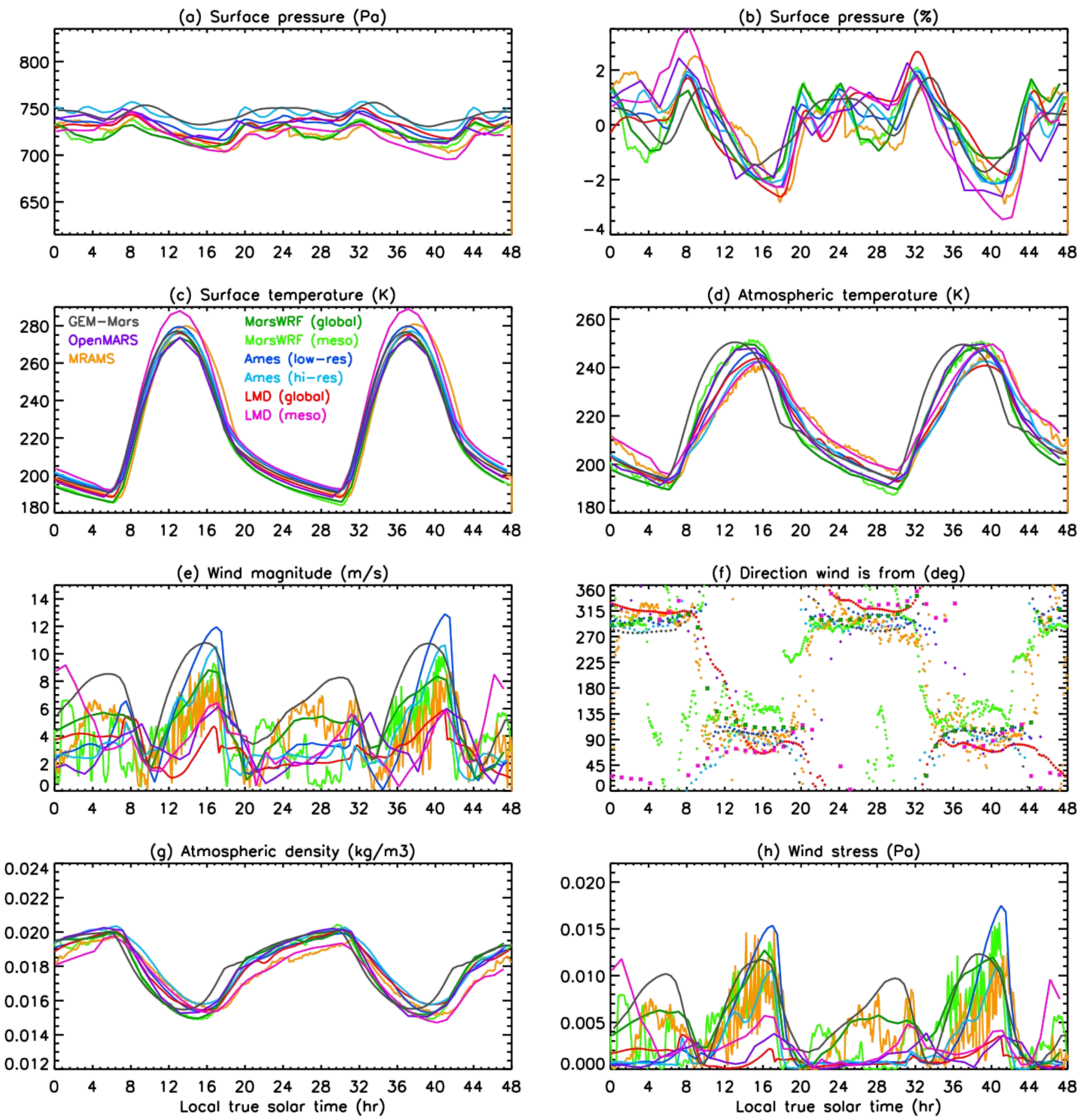

Figure 2.10: From Newman et al. (2020). Multi-model inter-comparison between seven models depicting the near-surface atmosphere on Mars. (e) refers to the wind magnitude simulations of each model including GEM-Mars, where the values are slightly higher than most other models during the night.

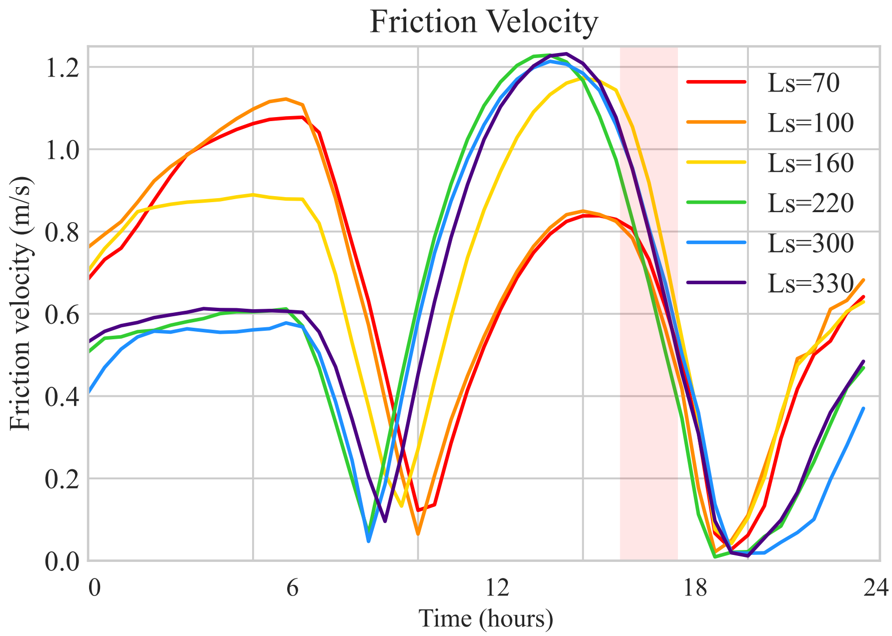

(a) Friction velocity

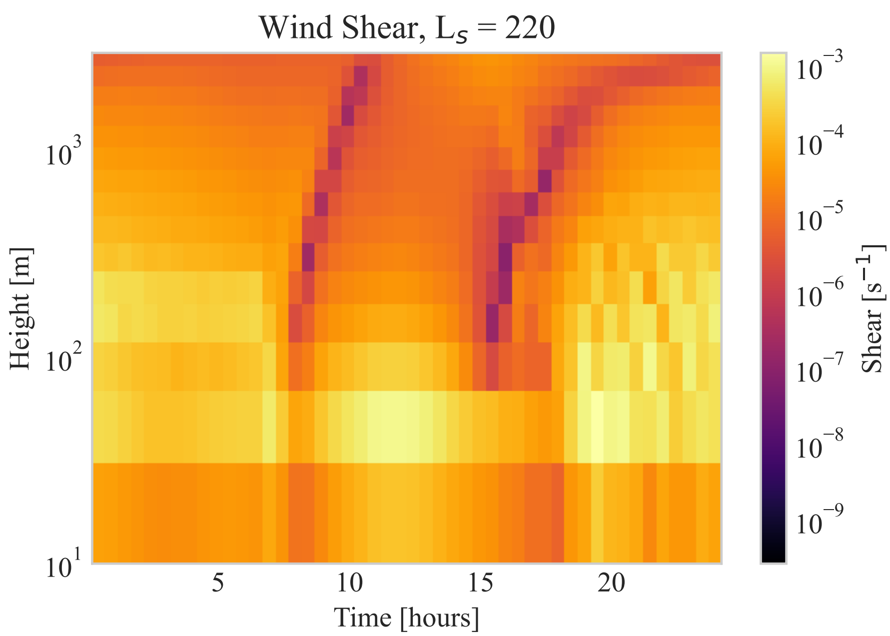

(b) Wind shear for $L_s = 220°$

Figure 2.11: (a) Friction velocity (u_*) from GEM-Mars outputs. u_* decreases to $\sim$ 0-0.2 m s^{-1} at sunrise, then begins to rise again through the day. It then begins to decrease at sunset, denoted by the vertical red line ($\sim$ 16:00 - 18:00) before steadily rising again through the night. (b) Wind shear from GEM-Mars outputs. Low values of wind shear correspond to higher gradient Richardson number values.

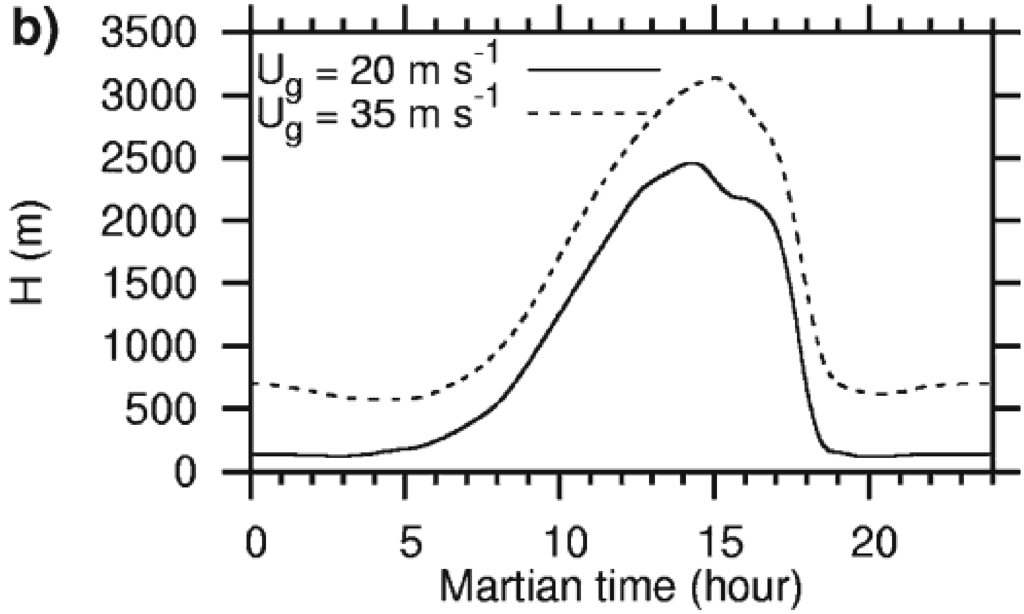

Figure 2.12: From Taylor et al. (2007). Modeled time variations of boundary layer depth given geostrophic winds of different speeds, showing a fast decrease at approximately 17:00-18:00.

experience reduced wind shear, causing a decrease in the height of the boundary layer. As a consequence, the gradient Richardson number, calculated by dividing by the wind shear (eq. 2.13), increases, leading to a decrease in turbulence levels and the establishment of stable stratification within the layers.

This sharp decrease can also be seen in Taylor et al. (2007), in which the PBL experiences a decrease in height at around 17:00 (Fig. 2.12). Conversely, higher values of wind shear indicate smaller gradient Richardson numbers, which can increase the turbulence in the atmosphere and create regions of convective instability. Note that the wind shear values shown here are computed from post-processed GEM-Mars outputs, rather than computed instantaneously along with diffusion coefficients. The wind shear values indicate regions of increased atmospheric instability and provide qualitative insights as to the physical mechanisms responsible for the diurnal variations in diffusivity identified in this study, but should not be interpreted as quantitative predictions of wind shear on Mars.

2.3.2 Model Limitations and Error Analysis

Though the model was run for up to 20 repetitions of a single sol, the spin-up required for a more accurate amount may require more repetitions. Less model spin-up showed less accurate results, though the equilibrium was met faster using background mixing ratios such that the model does not start with an abundance of zero.

Furthermore, compared to other General Circulation Models (GCMs) such as the Mars Weather Research and Forecasting Model (MarsWRF), GEM-Mars exhibits a lower spatial resolution, potentially encompassing information beyond Gale Crater. GEM-Mars operates at a resolution that does not capture all of the fine-scale atmospheric processes, leading to potential discrepancies between the model outputs and the actual reality of the Martian atmosphere. As such, the results presented in this study may be idealized and limited by the model resolution. Consequently, the limited spatial resolution of GEM-Mars restricts its ability to capture finer-scale processes and topographic features that could influence mixing and other related phenomena. Additionally, the turbulent parameterization scheme used in GEM-Mars is based on empirical relationships and assumptions, which may not always accurately capture the behavior of turbulent eddies in the Martian atmosphere.

Mischna et al. (2011) uses MarsWRF to characterize Martian methane release and its subsequent global mixing. Compared to the slightly larger grid size of GEM-Mars, MarsWRF uses a grid size of $1.25^\circ \times 1.25^\circ$ (~75 km resolution at the equator), with 40 vertical levels ranging up to 80 km in altitude, though Mischna et al. (2011) cites additional tests for a resolution of $5^\circ \times 5^\circ$. Their study used MarsWRF to then independently track the evolution of a plume of methane by changing several parameters including the release source location and season, emission duration, source strength, and tracer lifetime. Their study found that the behaviour of a methane plume is affected by the model resolution such that as the resolution becomes more coarse, the effects of numerical diffusion are more expansive and thus less accurate. For our study, the numerical diffusion is completed in the 1D model, though the outputs from GEM-Mars may be less accurate due to the resolution of the model.

Chapter 3

Water Vapor Condensation In Optical Instruments

3.1 Methods

In this section, we aim to investigate the water frost point as a crucial parameter for optimizing the performance of an instrument designed to measure methane at high frequencies. While the sensitivity of the instrument relies on cooler temperatures, it is essential to prevent frost from condensing in the analyzer cell, which would decrease the sensitivity and potentially damage the instrument. Therefore, an understanding of the water frost point allows us to identify regions where the instrument is most sensitive.

In Chapter 2, we explored the diurnal vertical evolution of methane in Gale Crater using model outputs from a GCM paired with a vertical diffusion model. Building upon these results, we aim to integrate in-situ diurnal methane observations with model data, allowing us to gain a more comprehensive understanding of the methane cycle on Mars. We use the ABB Inc. OA-ICOS instrument as a model instrument capable of taking hourly methane measurements. However, it is crucial to address the potential challenges associated with instrument performance and maximize its precision while safeguarding against frost-related issues. Thus, we calculate the maximum water frost point on the Martian surface to evaluate the highest risk scenario for frost forming in an instrument such as the OA-ICOS.

The frost point at any location and time is determined using temperature and water vapor column density data gathered from the Mars Climate Database (MCD) version 5.3 based on the general circulation model developed at the Laboratoire de Météorologie Dynamique (Forget et al., 2006; Lewis et al., 1999). The MCD has a spatial resolution of $5.625° \times 3.75°$, and is able to interpolate to a higher resolution using MOLA topography paired with smoothed Viking Lander 1 pressure records. This interpolation allows for the calculation of high resolution values of atmospheric variables, including areas of the map that are smaller than the original resolution, such as Gale Crater.

To calculate the frost point over the entire planet at a given solar longitude, the water vapor mixing ratio was taken over the entirety of the Martian surface at each hour of the day throughout Mars year 36. Each hour corresponds to a Martian hour, defined as lasting $1/24^{th}$ of a Martian day (sol). We then focused on five locations: Hellas Planitia, Gale Crater, the Viking 2 Lander site, the Phoenix Lander site, and the Tharsis region. Gale Crater, at 4.5° S, 137.4° E, is chosen as an equatorial location due to previous observations of atmospheric methane being reported by the Tunable Laser Spectrometer-part of the Sample Analysis at Mars (SAM-TLS) laboratory suite aboard NASA's Curiosity Rover (Webster et al., 2018), making the location a prime candidate for future missions to observe the methane cycle with optical instrumentation. The Viking 2 Lander site, at 48° N, 225.7° W, was chosen as a mid-latitude locations, and the Phoenix Lander site, at 68.2° N, 234.2° E was

Table 3.1: Coordinates chosen for each example location

Location	Center Coordinates
Gale Crater	(4.5° S, 137.4° E)
Phoenix Lander Site	(68.2° N, 234.2° E)
Viking 2 Lander Site	(48° N, 225.7° W)
Hellas Planitia	(40° S, 70° E)
Tharsis	(15° N, 235° E)

chosen as a polar location. Hellas Planitia, at 40° S, 70° E, is chosen as a mid-latitude site of low elevation, which impacts the local water vapor abundance, while Tharsis, centered at 15° N, 235° E, was chosen as an example of a region of high elevation. The coordinates for each site were constrained within the MCD and data at each site was taken every six Martian hours per solar longitude, every 20 solar longitudes over one full year. We assume frost formation happens when the atmosphere is saturated.

For each location, we use the MCD to spatially constrain the area with the relevant boundaries of the coordinate location. The coordinates for each location are highlighted in Table 1.

A grid of water vapor mixing ratios retrieved from the MCD was then generated for each location at 1 m in altitude, with a value at each coordinate within the boundaries. The maximum value within this region represents the highest frost point threshold and is thus the highest risk of frost. The frost point is calculated from the partial pressure of water in Pa, p_{water}, given by:

$$p_{water} = wP \tag{3.1}$$

Where w is the water vapor volume mixing ratio (mol/mol) obtained from the MCD (Forget et al., 2006; Lewis et al., 1999), and P is the air pressure in Pa. Values of p_{water} show a diurnal maximum of approximately 0.9 Pa at the Phoenix Lander location during $L_s = 100°$, which is consistent with the values obtained by the Phoenix thermal and electrical conductivity probe (TECP) relative humidity (RH) sensor (Fischer et al., 2019). Values of partial pressure derived from the RH of TECP varied diurnally from ∼0.01 Pa at 03:00 to ∼1 Pa at 12:00 during the same solar longitude. The frost points are found using the partial pressure of water vapor found in (1) with the Marti and Mauersberger equation for vapor pressure over ice (Marti & Mauersberger, 1993, Eq. 1):

$$\log_{10} p_{water} = -2663.5/T_f + 12.537 \tag{3.2}$$

$$T_f = \frac{2663500}{12537 - 1000\log(p_{water})} \tag{3.3}$$

In which T_f is the frost point (K). The Marti and Mauersberger equation is used for this study, as it has been validated for measurements of vapor pressure over ice for temperatures down to 170K, which is within the range of Martian surface temperatures and is lower than the minimum validated temperatures of other frost point formulations (Marti & Mauersberger, 1993). Since the carbon dioxide frost point is lower than the water frost point everywhere on Mars at all times (Schorghofer & Edgett, 2006), we focus solely on the water frost point, as the warmest temperature at which volatile condensation occurs is a concern. The frost point is calculated over one Mars year for five locations: Hellas Planitia, the Tharsis region, Gale Crater, the Viking 2 Lander site, and the Phoenix Lander site.

3.1.1 Model Instrument

As a model instrument, this paper considers a trace-gas spectrometer currently under development for use on the surface of Mars. The ABB Inc. OA-ICOS instrument has a small gas cell with extremely reflective mirrors (>0.9999 reflectivity) to

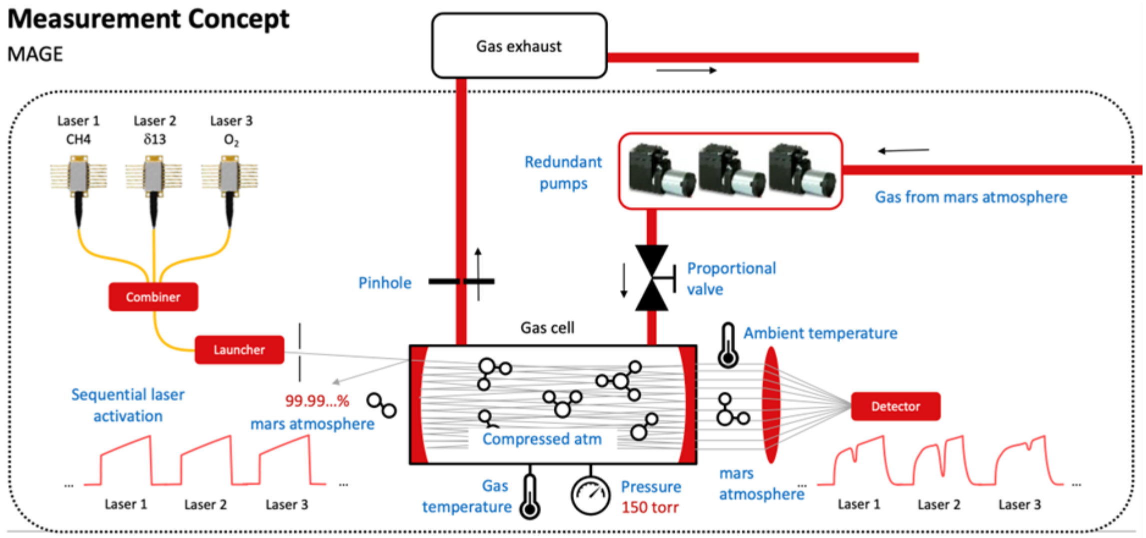

Figure 3.1: Provided by ABB Inc., a schematic of the MAGE system based off the ABB Inc. OA-ICOS. The heart of the system is a gas cell bounded by extremely reflective mirrors which must reflect each photon tens of thousands of times to produce the required performance. As such, any marring of those mirrors by condensation can substantially degrade the precision of the instrument, making it unable to meaningfully measure trace gas concentrations.

create a mean optical path for each photon of greater than a kilometer (Fig. 3.1). This path length is more than 60 times longer than that of SAM-TLS which has a path length of 16.8 m (Mahaffy et al., 2012). The exceptionally long optical path length means that this instrument, and others like it, can measure very low concentrations of several trace gasses at concentrations of as little as a fraction of one part per billion by volume (ppbv) in minutes without requiring any pre-processing or enrichment steps. This instrument is more precise at low temperatures for two reasons. First, when the detector and electronics are as cold as possible, thermal noise is minimized, improving the instrument's signal-to-noise (SNR) ratio. Secondly, at colder temperatures the density of gas within the fixed volume gas cell will be higher at the same pressure, allowing for more absorption without pressure broadening the absorption lines that are measured (Fig. 3.2). As the temperature increases, the

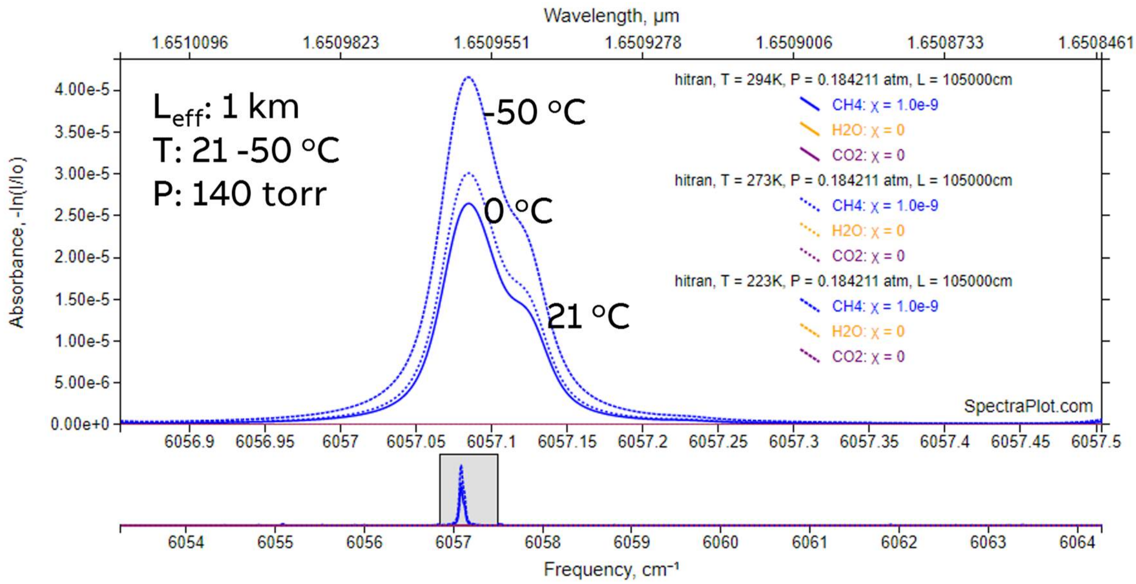

Figure 3.2: Provided by ABB Inc., the effect of temperature change for spectroscopic analysis. As temperatures within the analyzer cell decrease, the wavelength range decreases, increasing the signal.

interval between collisions decreases, and the broadening is more pronounced. The wavelength in which absorption lines will be measured for methane is in the infrared range (780 nm to 10 μm). As such, for pressure broadening in the infrared range, the Lorentz line shape width and depth are inversely proportional to the temperature such that as the temperature increases, the absorption signal decreases (Andrews, 2010, p. 3.21). For pressure broadening in the infrared range, the Lorentz line shape is given by:

$$f(\nu - \nu_n) = \left(\frac{\gamma_L}{\pi}\right) \frac{1}{(\nu - \nu_n^2) + \gamma_L^2}, \tag{3.4}$$

where the half-width at half maximum is $\gamma_L = (2\pi\tau_c)^{-1}$. Collisional lifetime is τ_c, which, along with γ_L, are obtained in terms of mean molecular velocity which is proportional to $T^{1/2}$ (Andrews, 2010).

While this system is mechanically robust, any condensation within the gas cell that affects the reflectivity of the mirror would result in reduced performance. Because each photon reflects off each mirror tens of thousands of times during a measurement, even subtle marring or degradation of the mirror surfaces can result in greatly decreased performance. Instruments similar to the OA-ICOS that are employed for sensitive measurements of gas samples on the Martian surface should ensure careful consideration of potential issues related to frost deposition, using temperature regulation and internal heaters to prevent frost formation.

3.2 Results

The distribution of atmospheric water vapor follows both meridional and zonal patterns as the seasons change, with higher abundance in the north polar region during northern summer (Fig. 3.3b), and in the south pole during southern summer (Fig. 3.3d). The polar ice caps play a significant role in shaping the global and seasonal distribution of atmospheric water vapor; as the ice caps melt, more water content becomes available to the entire planet (Fedorova et al., 2006; Smith, 2002; Smith et al., 2009). Consequently, the Phoenix Lander location experiences the highest frost point maximums during northern spring and summer due to the increased supply of atmospheric water near the north pole during these seasons. Conversely, the lowest maximums are observed in the polar regions during their respective winters (e.g., L_s = 270° for northern winter and L_s = 90° for southern winter) when the ice caps grow once more. This is consistent with the Mars Express/OMEGA (Observatoire pour la Minéralogie, l'Eau, les Glaces et l'Activité) observations during L_s = 94°- 145°, in which water frost has been detected at mid-latitude regions (Bibring et al., 2004).

During northern spring and fall (Fig. 3.3a,c), the frost point is the lowest near the north and south poles respectively, again due to the atmospheric water abundance.

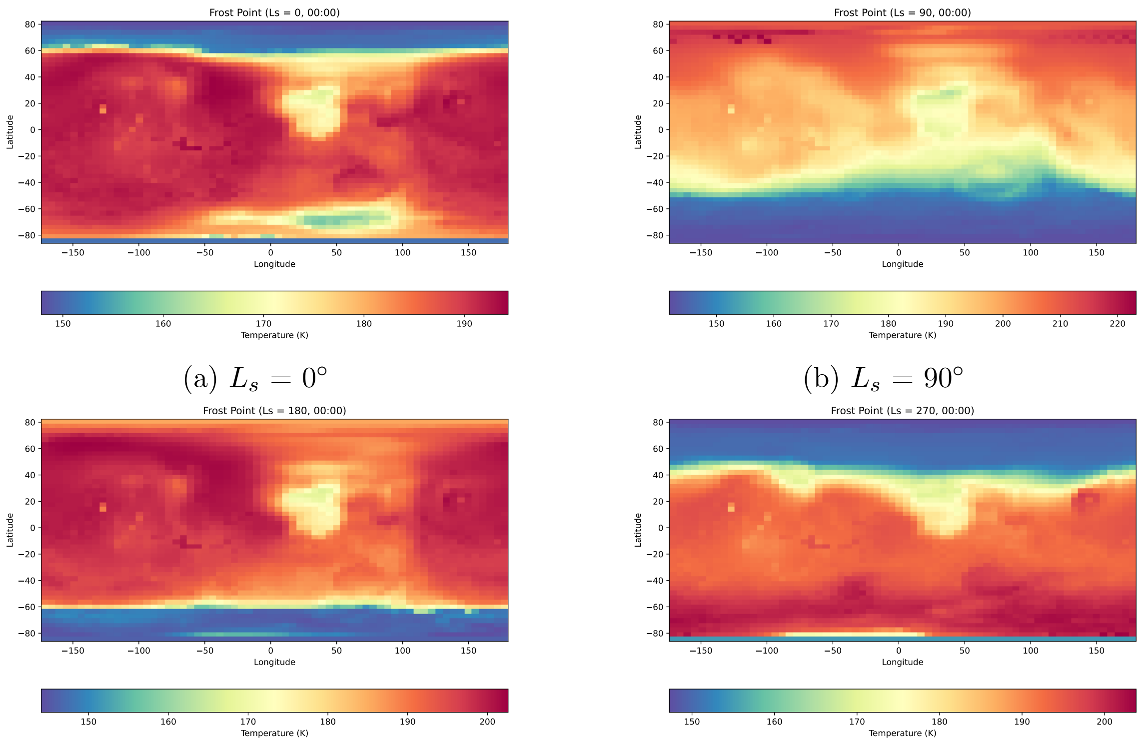

(a) $L_s = 0°$

(b) $L_s = 90°$

(c) $L_s = 180°$

(d) $L_s = 270°$

Figure 3.3: Frost point temperatures at $L_s = 0$, 90, 180, and 270° calculated from water vapor mixing ratios gathered from the MCD (Forget et al., 2006; Lewis et al., 1999). The highest temperatures appear at around the Hellas Planitia (40° S, 290° W) region during $L_s = 0$ and 180°, the north pole during $L_s = 90°$ (northern summer), and the south pole during $L_s = 270°$ (northern winter).

During northern summer and winter (Fig. 3.3b,d), the frost point exhibits the highest and lowest maximums respectively solely in the polar regions with areas of low elevation in equatorial and mid-latitude regions having less of an effect. Near Arabia Terra (~20° N, 30° E), lower frost point values indicate a lower water vapor abundance near midnight. Pál et al. (2019) shows that the water vapor mixing ratio drops more rapidly in areas such as Arabia Terra, which are more humid during the day, indicating that water vapor may deposit near and on the surface during the night.

Figure 3.4 shows the temperature differential between the air temperature and the frost point across the entire surface, where any difference less than zero is where frost can form given the local water vapor mixing ratio. Air temperatures are taken at a Local True Solar Time ($LTST_0$) of 00:00, where $LTST_0$ is the local time at longitude 0. As air temperatures decrease, the likelihood of water vapor condensation rises. Areas where the difference is greater than zero has less of a chance of frost forming, with higher differences indicating less of a risk of frost, though instruments that rely on colder temperatures for higher precision will lose precision due to temperatures being higher. The maximum precision of such instruments is achieved in areas where the temperature difference is closest to, but not less than, zero. Moreover, the surface cooling due to radiative processes during the night leads to the cooling of the overlying air. Therefore, instruments positioned closer to the surface have a higher risk of encountering frost during the night.

Throughout the year, the frost point exhibits variations depending on the season and latitude (Fig. 3.5), resulting in a wider range of temperatures around the Phoenix Lander site located in the polar region, and a smaller range near Gale Crater, situated closer to the equator. The frost point at the Phoenix Lander location over one year show a highest maximum of 212 K during early northern summer. For the Hellas Planitia frost point maximums, values decrease down to $\sim$188 K during northern spring, contrasting to the other regions which exhibit higher mean frost point values during northern spring and summer. Lower frost point maximums are seen at mid-latitude and equatorial regions during northern spring and summer in contrast to the Phoenix lander site in the polar region, whereas the frost point maximums at mid-latitude and equatorial regions during northern fall and winter increase to values above that of the polar region. At the Gale Crater site, the frost point values stay within a smaller range and reaches a maximum in the northern summer, though they remain relatively more constant throughout the year in comparison to the frost

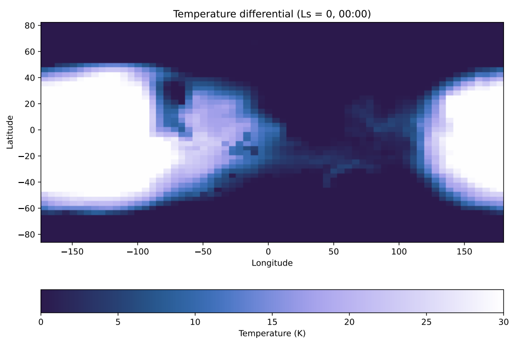

(a) $L_s = 0°$

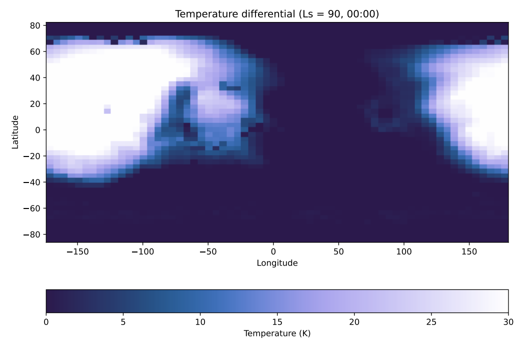

(b) $L_s = 90°$

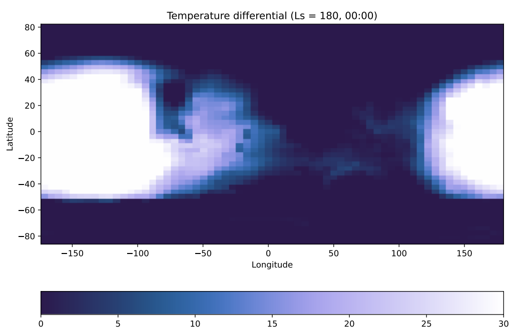

(c) $L_s = 180°$

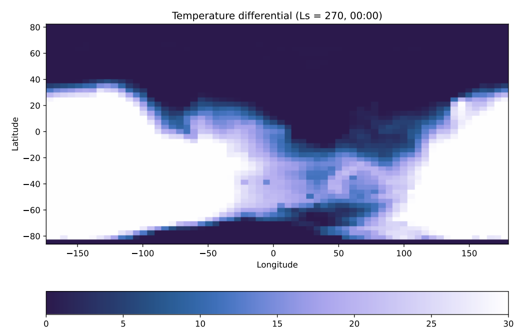

(d) $L_s = 270°$

Figure 3.4: Temperature differential between ambient surface temperatures and frost point. Areas of the plot where the values are at zero are areas where the air temperature is equal to or less than the frost point during $\mathrm{LTST}_0 = 00{:}00$ (at longitude 0 such that the local time at Gale Crater is 09:00). During the daytime the difference between frost point and air temperature is larger, and during night the air temperature reaches the frost point.

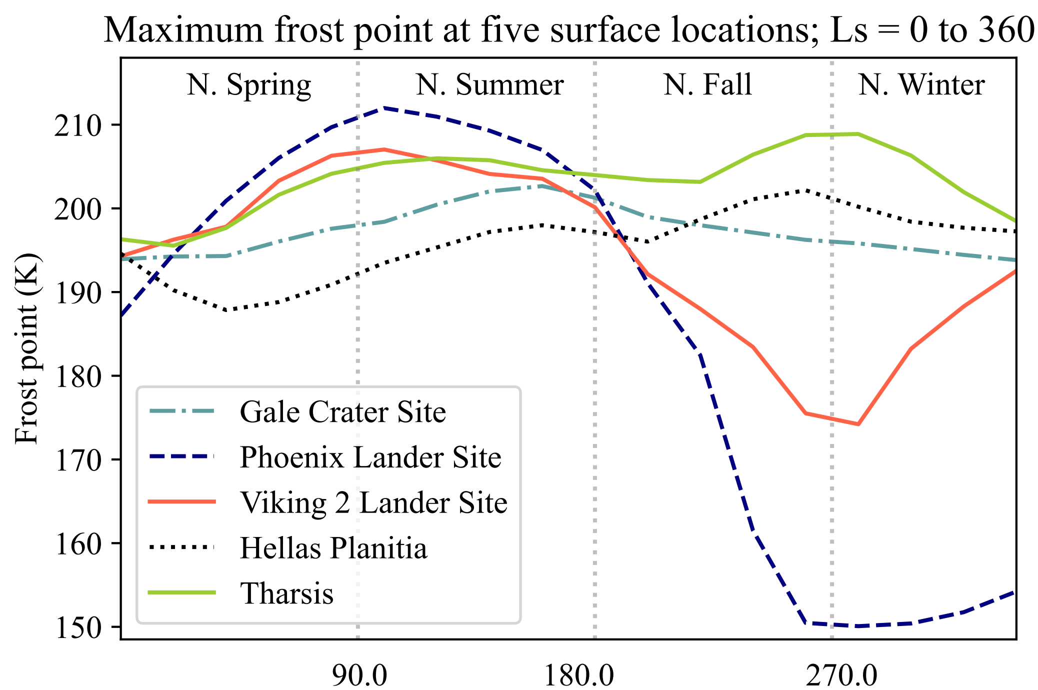

Figure 3.5: Frost point though one Martian year at five locations. The light blue dot-dashed line shows the frost point at the Gale Crater location, the dark blue dashed line shows the frost point at the Phoenix landing site, the red solid line shows the frost point at the Viking 2 lander site, the black dotted line shows the frost point at Hellas Planitia, and the green solid line shows the frost point at Tharsis. All locations except Hellas Planitia and Tharsis show a maximum peak in northern summer (L_s = 90°-180°), and a minimum in northern winter (L_s = 270°-360°). Hellas Planitia and Tharsis show a maximum peak in northern fall, and a minimum in northern spring.

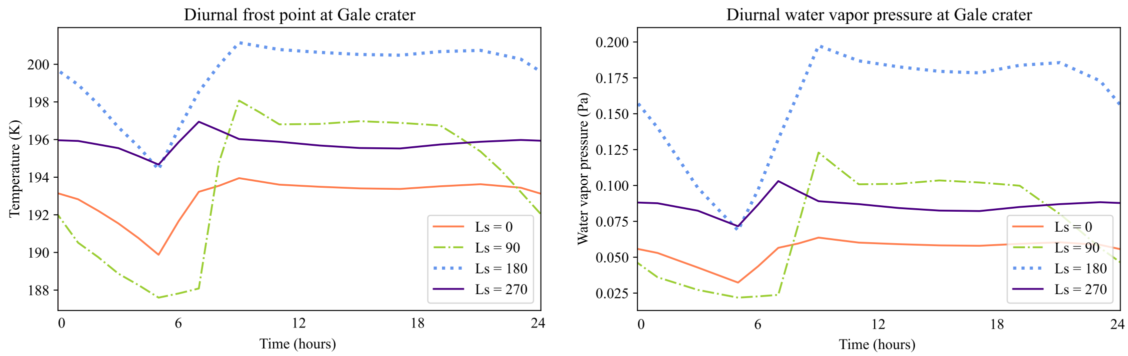

Figure 3.6: Frost point (left) and water vapor pressure (right) though one sol at Gale Crater during $L_s = 0°$, $90°$, $180°$, and $270°$. Highest values for both frost point and water vapor pressure are seen during $L_s = 180°$, when the water vapor abundance at Gale Crater is increased relative to during $L_s = 0°$, $90°$, and $270°$. Both the frost point and water vapor pressure during each solar longitude begins to decrease after sunset, and then increase around sunrise (∼06:00).

point maximums at the Phoenix Lander location. The Viking 2 Lander site shows a wider range of frost points throughout the year than Gale Crater and Hellas Planitia, though the variation not as extreme as at the Phoenix Lander location.

As the water vapor abundance decreases in the mid-latitude range from $L_s = 100°$-$360°$, the frost point at each location besides Hellas Planitia reaches a low during northern winter ($L_s = 270°$-$360°$), where an instrument may be kept at a lower temperature. At Gale Crater, where the water vapor abundance experiences less of a variation, the frost point ranges from approximately 193 K to 202 K and reaches a maximum during northern summer at around $L_s = 130°$. Similarly, the frost point at the Tharsis region experiences less variation during most of the year, though the frost point increases to ∼208 K during northern fall and winter.

The Tharsis region is an elevated plateau which features three volcanoes, the tallest of which reaches 18 km in elevation. This topography suggests low water vapor content at the peaks of the volcanoes, but a relatively higher amount at the bases, giving a similar frost point maximum to that at Gale Crater. At the Phoenix Lander location, where the water vapor abundance has a larger variation over the year, the frost point exhibits a larger range from approximately 150 K to 212 K, peaking during early northern summer and reaching a minimum near the end of northern winter. The Viking 2 Lander site shows a frost point range from to 174 K to 207 K, also reaching a maximum near the beginning of northern summer, and a minimum during mid-winter.

The diurnal variation in the frost point and water vapor pressure for Gale Crater are shown in Fig. 3.6 for $L_s = 0°$, 90°, 180°, and 270°. Values of p_{water} range between approximately 0.021 Pa ($T_f \sim$187 K) and 0.20 Pa ($T_f \sim$201 K), on $L_s = 90°$ at ∼06:00, and $L_s = 180°$ at ∼09:00 respectively. During $L_s = 0°$, when Gale Crater is drier relative to other seasons, the frost point ranges from ∼189 to ∼194 K which is a smaller range of values than for $L_s = 90°$ and $L_s = 180°$. Conversely, the frost point reaches a higher maximum during $L_s = 180°$ at the beginning of southern spring when the water vapor abundance is higher. During the day, the frost point maximums for $L_s = 0°$ are lower than during the other solar longitudes, however the lowest maximums are seen before sunrise during $L_s = 90°$ as temperatures decrease and water vapor is deposited onto the surface. The frost point at each solar longitude experiences a decrease over night and increases around sunrise, staying relatively higher throughout the day.

3.3 Discussion

3.3.1 Optimal scenario for sensitive measurements

For a year-long mission, instruments such as the OA-ICOS would need to be kept well above the frost point of the location at which the instrument is placed so water does not condense within the analyzer cell. As the frost point decreases, the instrument will be able to make more precise measurements, requiring smaller amounts of gas concentrations for measuring. If frost does occur, it is likely that gas analyzers may be susceptible to functional impairments, such as decreased internal valve, dust filter, and pump performance, as well as reduced signal strength caused by insufficient reflection and transmission of light through the optics. Given the potential for condensing water inside the analyzer cell, it is essential to take into account these seasonal frost point maximums.

The frost point of water is shown to vary seasonally, reaching the highest maximums during northern summer at three geographic areas: Gale Crater, the Viking 2 Lander site, and the Phoenix Lander Site. Hellas Planitia and Tharsis experience the highest frost point maximums during northern fall. The water vapor column plays a key role in the temperature at which water condenses, and the latitude and topography of the surface affects the areas at which the frost point maximums increase or decrease. The frost point of water in these example regions demonstrate the temperature above which a sample gas analyzer instrument would need to be held above.

The Phoenix Lander frost point values can be compared with the frost point values obtained by the Phoenix TECP and RH sensor (Fischer et al., 2019). Values of frost point recorded by TECP are provided for $L_s = 70°$-$180°$, and average to approximately 207 K during the day, though values up to 215 K are measured during $L_s = 101°$. Fischer et al. (2019) uses the frost point equation by Buck (1981) to calculate the water vapor pressure with respect to ice. Frost point values obtained by different equations such as Wagner et al. (2011) yield similar results, with a maximum difference in water vapor pressure values of 0.8%. The highest values of p_{water} measured by TECP were recorded between $L_s = 104°$ - $118°$, which correspond to the highest frost point maximums in this study. After $\sim L_s = 128°$, maximum diurnal values of p_{water} measured by TECP begin to decrease as temperatures drop, which is also seen in this study as frost point values begin to decrease during the same time.

With the seasonal frost point variation, the best opportunity to reach a minimum temperature without the risk of condensing water within an instrument, would be during northern fall and winter ($L_s = 180°$-$360°$), before the frost point begins to rise again. The latitude and elevation of a location should be taken into account when choosing the location for high-sensitivity spectrometers, with the seasonal variation of the water vapor column taken into account. Unlike in equatorial regions, the frost point in the polar regions experiences less correlation with topography and experiences a larger decrease in frost point from the minimal amount of atmospheric water vapor abundance.

3.3.2 Model Limitations

It is important to acknowledge the limitations of the MCD in the context of this study. The MCD employs models and parameterizations to simulate the Martian atmosphere, which can introduce uncertainties in the accuracy of the results obtained (Forget et al., 1999; Forget et al., 2014; Millour et al., 2017). The techniques presented in this paper are subject to several limitations due to the constraints of the MCD, which averages model outputs over twelve times a year and twelve times a day and thus cannot represent the full range of model variability. Additionally, data may be linearly interpolated, ensuring maximum and minimum values will not, in general, be reflected in the outputs. Consequently, the calculated frost point values may differ from the actual values due to the limitations of the water vapor mixing ratios provided by the MCD. Future missions that rely on cold temperatures for more sensitive measurements may need additional model runs and in-situ data to ensure a more accurate estimation of the water frost point threshold.

3.3.3 Implications of internal compression and expansion

Many gas analyzer instruments and spectroscopy techniques are sensitive to the pressure within the analyzer cell. Consequently, the pressure within an analyzer cell may need to be higher than the Martian surface pressure. As a sample of gas is compressed adiabatically to reach the internal pressure of the instrument, the internal temperature would increase to temperatures well above the frost point. Although this would mitigate the risk of frost deposition, depending on the internal pressure, the temperature may rise significantly. In an adiabatic process, the temperature of the compressed gas is related to the pressure and the ambient conditions by the following equation:

$$T_2 = \frac{T_1 {p_1}^{\frac{(1-\gamma)}{\gamma}}}{{p_2}^{\frac{(1-\gamma)}{\gamma}}} \tag{3.5}$$

Where T_2 is the temperature after adiabatic compression, T_1 is the ambient air temperature, p_1 is the ambient pressure, p_2 is the pressure to which the cell is compressing, and $\gamma = 1.28$ is the heat capacity ratio for CO_2. Given an air temperature of 200 K at Gale Crater, when the frost point is at or above this temperature, and a surface pressure of 790 Pa, if the typical internal pressure of the instrument is 15,000 Pa and the gas sample is allowed to adiabatically compress, the internal temperature would reach approximately 380 K. Furthermore, once the sample reaches thermal equilibrium and then is allowed to cool adiabatically again when vented, the internal temperature would drop to approximately 105 K, where frost deposition of both water and CO_2 would occur. Should the instrument heat or cool non-adiabatically, in which compression or decompression is done slowly to minimize the temperature change, water will be condensed, and frost deposition will be guaranteed. Future missions should take into account internal compression and adiabatic heating of gas samples such that no deposition occurs, but temperatures remain within the limitations of the instrument.

Chapter 4

Conclusions

4.1 Methane Modeling

The work presented in this thesis investigates the vertical evolution of methane background seepage within the Martian PBL using a one-dimensional diffusion model coupled with outputs from GEM-Mars. We focused on finding the surface emission fluxes and vertical evolution of methane concentrations using modeling techniques to replicate the methane measurements obtained by SAM-TLS. By incorporating GEM-Mars outputs which simulate atmospheric diffusion, we are able to reproduce the observed methane concentrations with a given initial surface flux. Surface emission fluxes play a crucial role in providing information about the exchange of methane between the surface and the atmosphere. As such, we can use surface fluxes to quantify the amount of methane emitted from the planet's surface.

We used ten example solar longitudes (L_s=10°, 30°, 70°, 100°, 140°, 160°, 220°, 270°, 300°, 330°) which were closely matched to the solar longitudes during which SAM-TLS made measurements, including the same time of day the measurements were taken. We find the fluxes required to match the SAM-TLS measurements vary with time of year, as the diffusion coefficients change with solar longitude, which in turn affects the mixing ratios of methane at different heights in the atmosphere. This variation corresponds to the mixing ratio measured by SAM-TLS, with a maximum seen during the northern summer. We also find the methane mixing ratio varies with time of day, building up overnight when the PBL is collapsed and mixing is diminished, then diffusing more rapidly during the daytime as diffusion coefficients increase.

We compared model results of surface fluxes to that of approximated boundary layer heights (Moores et al., 2019b) and found model fluxes to be on average approximately one order of magnitude greater than the approximated values, though they are closer matched by a daily average of 1.5 x 10^{-10} kg m^{-2} sol^{-1}. One reason our values are higher may be attributed to the higher rates of diffusivity as modeled by GEM-Mars, which requires a higher surface flux to match the same concentration.

Overall, our study highlights the importance of accurate modeling of diffusion coefficients in understanding the behavior of methane on Mars. The modeled flux values shed light on the accumulation scale of methane in the atmosphere and emission timescale, considering microseepage contributions. Analyzing the vertical evolution of methane over the course of a day offers valuable insight into its variation at different altitudes and times. The high diffusivity within the PBL during the daytime enables methane to efficiently mix away, and in times of particularly low diffusivity, methane build-up increases to higher levels. Consequently, surface measurements and nighttime observations prove most advantageous for methane detection.

Further studies are needed to investigate the sources and sinks of methane on Mars and to refine our understanding of the diffusion processes involved. This will require more detailed observations and measurements from future missions, as well as continued improvements in our modeling capabilities.

To summarize, the work presented in this thesis finds:

- The vertical evolution and accumulation of methane throughout a day is influenced by atmospheric stability, where stable conditions lead to more methane accumulation near the surface

- Modeled values of eddy diffusivity are higher during the day resulting in lower methane mixing ratios, while lower diffusion coefficients during the night lead to higher methane mixing ratios, indicating the accumulation of methane over night and confirming a diurnal variation

- The fluxes required to reproduce the SAM-TLS methane measurements using GCM outputs paired with a vertical diffusion model exhibit a seasonal trend, with higher fluxes during northern summer

- The methane flux values are on average an order of magnitude larger in comparison with Moores et al. (2019b) due to higher diffusion coefficients from GEM-Mars

4.2 Frost Point

Our analysis reveals that the average frost point maximums in Gale Crater, where previous methane measurements have been made, stay relatively high through each season, including northern fall and winter, when the atmospheric water vapor content is less abundant though concentrated closer to Gale Crater. In contrast, the Phoenix Lander location experiences a more significant decrease in the frost point during those seasons. Gale Crater, the Phoenix Lander site, and the Viking 2 Lander site experience the highest frost point maximums during northern summer, while Hellas Planitia and Tharsis experience the highest maximums during the end of northern fall.

These results have important implications for high-sensitivity gas analyzers on any future mission to an equatorial or mid-latitude region. An instrument sent to Gale Crater to further conduct high-precision methane measurements will experience less of a risk of frost during northern spring and summer, compared to the Phoenix Lander location where the frost point maximums are higher. However, a larger methane sample will be required for analysis during the northern fall and winter months in Gale Crater, as the frost point will be higher than at the Phoenix Lander location, and therefore the instrument will not be able to cool as much, preventing higher precision. The frost point over a year at each example location was seen to vary from a low of 150 K at the Phoenix Lander location, up to 212 K, also at the same location, with equatorial and mid-latitude regions seeing less of a variation in frost point through the year. Future missions to Mars for gas analysis will have to take these ranges and the seasonal variation of frost point into account in order to achieve maximum precision while keeping the instrument free of frost.

Chapter 5

Future Work

The models described in Chapter 2.1 currently have no implemented destruction mechanism which would help to explain the behaviour of methane loss. By simulating methane destruction and sequestration in the vertical diffusion model, we would be able to assess the impact on methane abundances and this would allow us to explore the impact of chemical reactions or physical processes that would break methane down. The work reported by Moores et al. (2019a) considers adsorption onto and diffusion through the regolith. Incorporating subsurface mechanisms and diffusion through the regolith into our current model would add further context to the methane flux out of the surface. This can also extend to modeling methane spikes over 2 ppbv, which occur periodically and are usually isolated spatially. Spikes have been reported by instruments such as Curiosity (Webster et al., 2018; Webster et al., 2021), though spikes are usually only observed for a small amount of time after their release, suggesting fast destruction or sequestration. Modeling spike behavior and evolution would thus potentially give more insight to the sources and sinks of methane, and further characterize the methane cycle. Integrating future in-situ measurements from the OA-ICOS instrument would add additional data which could also be used as inputs in future modeling efforts.

Currently, our work is constrained to Gale Crater because of the measurements taken by SAM-TLS. Expanding the modeling work globally would allow us to use parameters from other locations on Mars to measure methane accumulation and the corresponding fluxes. Assuming Gale Crater is not unique in the release of methane, comparing the flux at Gale Crater with the flux at other locations on Mars could potentially provide more context to the low upper limit reported by TGO and how methane evolves vertically.

Furthermore, conducting a multi-model inter-comparison of diffusion coefficients and other key atmospheric processes, including wind shear, and their impact on the surface flux and evolution of methane would be valuable. An inter-comparison would offer valuable insights into the limitations and capabilities of different models, giving a better understanding of the fluxes and evolution of methane. In particular, comparing the fluxes calculated using MarsWRF diffusion coefficients, considering its higher resolution and differing diffusion characteristics, to those obtained using GEM-Mars would give a more accurate assessment of the uncertainties associated with calculating methane fluxes.

References

Andrews, D. G. (2010). *An introduction to atmospheric physics* (2nd ed.). Cambridge University Press. https://doi.org/10.1017/CBO9780511800788

Atreya, S., Wong, A.-S., Rennó, N., Farrell, W., Delory, G., Sentman, D., Cummer, S., Marshall, J., Rafkin, S., & Catling, D. (2006). Oxidant enhancement in martian dust devils and storms: Implications for life and habitability. *Astrobiology*, *6*, 439–50. https://doi.org/10.1089/ast.2006.6.439

Benson, J. L., Bonev, B. P., James, P. B., Shan, K. J., Cantor, B. A., & Caplinger, M. A. (2003). The seasonal behavior of water ice clouds in the tharsis and valles marineris regions of mars: Mars orbiter camera observations. *Icarus*, *165*(1), 34–52. https://doi.org/https://doi.org/10.1016/S0019-1035(03)00175-1

Bhattacharyya, D., Clarke, J., Bertaux, J.-L., Chaufray, J.-Y., & Mayyasi, M. (2015). A strong seasonal dependence in the martian hydrogen exosphere. *Geophysical Research Letters*, *42*, n/a–n/a. https://doi.org/10.1002/2015GL065804

Bibring, J. P., Soufflot, A., Berthé, M., Langevin, Y., Gondet, B., Drossart, P., Bouyé, M., Combes, M., Puget, P., Semery, A., Bellucci, G., Formisano, V., Moroz, V., Kottsov, V., Bonello, G., Erard, S., Forni, O., Gendrin, A., Manaud, N., . . . Ignatiev, N. (2004). OMEGA: Observatoire pour la Minéralogie, l'Eau, les Glaces et l'Activité. In A. Wilson & A. Chicarro (Eds.), *Mars express: The scientific payload* (pp. 37–49).

Bibring, J.-P., Langevin, Y., Mustard, J. F., Poulet, F., Arvidson, R., Gendrin, A., Gondet, B., Mangold, N., Pinet, P., Forget, F., Berthé, M., Bibring, J.-P., Gendrin, A., Gomez, C., Gondet, B., Jouglet, D., Poulet, F., Soufflot, A., Vincendon, M., . . . Neukum, G. (2006). Global mineralogical and aqueous mars history derived from omega/mars express data. *Science*, *312*(5772), 400–404. https://doi.org/10.1126/science.1122659

Briggs, G., Klaasen, K., Thorpe, T., Wellman, J., & Baum, W. (1977). Martian dynamical phenomena during june–november 1976: Viking orbiter imaging results. *Journal of Geophysical Research*, *82*(28), 4121–4149.

Buck, A. L. (1981). New equations for computing vapor pressure and enhancement factor. *Journal of Applied Meteorology and Climatology*, *20*(12), 1527–1532. https://doi.org/https://doi.org/10.1175/1520-0450(1981)020<1527:NEFCVP>2.0.CO;2

Carrozzo, F., Bellucci, G., Altieri, F., D'Aversa, E., & Bibring, J.-P. (2009). Mapping of water frost and ice at low latitudes on mars. *Icarus*, *203*(2), 406–420.

Chassefière, E. (2009). Metastable methane clathrate particles as a source of methane to the martian atmosphere. *Icarus*, *204*(1), 137–144. https://doi.org/https://doi.org/10.1016/j.icarus.2009.06.016

Christensen, P. R., Bandfield, J. L., Hamilton, V. E., Ruff, S. W., Kieffer, H. H., Titus, T. N., Malin, M. C., Morris, R. V., Lane, M. D., Clark, R. L., Jakosky, B. M., Mellon, M. T., Pearl, J. C., Conrath, B. J., Smith, M. D., Clancy, R. T., Kuzmin, R. O., Roush, T., Mehall, G. L., . . . Greenfield, M. (2001). Mars global surveyor thermal emission spectrometer experiment: Investigation description and surface science results. *Journal of Geophysical Research: Planets*, *106*(E10), 23823–23871. https://doi.org/https://doi.org/10.1029/2000JE001370

Cicerone, R. J., & Oremland, R. S. (1988). Biogeochemical aspects of atmospheric methane. *Global Biogeochemical Cycles*, *2*(4), 299–327. https://doi.org/https://doi.org/10.1029/GB002i004p00299

Cooper, B., de la Torre Juárez, M., Mischna, M., Lemmon, M., Martínez, G., Kass, D., Vasavada, A. R., Campbell, C., & Moores, J. (2021). Thermal forcing of the nocturnal near surface environment by martian water ice clouds [e2020JE006737 2020JE006737]. *Journal of Geophysical Research: Planets*, *126*(12), e2020JE006737. https://doi.org/https://doi.org/10.1029/2020JE006737

Fassett, C. I., & Head, J. W. (2008). Valley network-fed, open-basin lakes on mars: Distribution and implications for noachian surface and subsurface hydrology. *Icarus*, *198*(1), 37–56. https://doi.org/https://doi.org/10.1016/j.icarus.2008.06.016

Fedorova, A., Korablev, O., Bertaux, J.-L., Rodin, A., Kiselev, A., & Perrier, S. (2006). Mars water vapor abundance from spicam ir spectrometer: Seasonal and geographic distributions. *Journal of Geophysical Research: Planets*, *111*(E9). https://doi.org/https://doi.org/10.1029/2006JE002695

Fischer, E., Martínez, G. M., Rennó, N. O., Tamppari, L. K., & Zent, A. P. (2019). Relative humidity on mars: New results from the phoenix tecp sensor. *Journal of Geophysical Research: Planets*, *124*(11), 2780–2792. https://doi.org/https://doi.org/10.1029/2019JE006080

Fonseca, R. M., Zorzano-Mier, M.-P., & Martín-Torres, J. (2018). Planetary boundary layer and circulation dynamics at gale crater, mars. *Icarus*, *302*, 537–559. https://doi.org/https://doi.org/10.1016/j.icarus.2017.11.036

Forget, F., Millour, E., Lebonnois, S., Montabone, L., Dassas, K., Lewis, S., Read, P., López-Valverde, M., González-Galindo, F., Montmessin, F., et al. (2006). The new mars climate database.

Forget, F., Hourdin, F., Fournier, R., Hourdin, C., Talagrand, O., Collins, M., Lewis, S. R., Read, P. L., & Huot, J.-P. (1999). Improved general circulation models of the Martian atmosphere from the surface to above 80 km. *Journal of Geophysical Research*, *104*(E10), 24155–24176. https://doi.org/10.1029/1999JE001025

Forget, F., Millour, E., Spiga, A., Madeleine, J.-B., Pottier, A., Navarro, T., Colaitis, A., Kerber, L., Lefèvre, F., Montmessin, F., Chaufray, J.-Y., Gonzalez-Galindo, F., Montabone, L., Lopez-Valverde, M., Lewis, S., & Read, P. L. (2014). Simulating the Mars Climate with the LMD Mars Global Climate Model: validation and issues. In F. Forget & M. Millour (Eds.), *The Fifth International Workshop on the Mars Atmosphere: Modelling and Observations* (p. id.1204). https://hal.science/hal-01139581

Formisano, V., Atreya, S., Encrenaz, T., Ignatiev, N., & Giuranna, M. (2004). Detection of methane in the atmosphere of mars. *Science (New York, N.Y.)*, *306*, 1758–61. https://doi.org/10.1126/science.1101732

Geminale, A., Formisano, V., & Giuranna, M. (2008). Methane in martian atmosphere: Average spatial, diurnal, and seasonal behaviour. *Planetary and Space Science*, *56*(9), 1194–1203. https://doi.org/https://doi.org/10.1016/j.pss.2008.03.004

Giuranna, M., Viscardy, S., Daerden, F., Neary, L., Etiope, G., Oehler, D., Formisano, V., Aronica, A., Wolkenberg, P., Aoki, S., Cardesin-Moinelo, A., Marín-Yaseli de la Parra, J., Merritt, D., & Amoroso, M. (2019). Independent confirmation of a methane spike on mars and a source region east of gale crater. *Nature Geoscience*, *12*. https://doi.org/10.1038/s41561-019-0331-9

Gloesener, E., Karatekin, Ö., & Dehant, V. (2021). Stability and composition of ch4-rich clathrate hydrates in the present martian subsurface [From Mars Express to Exomars]. *Icarus*, *353*, 114099. https://doi.org/https://doi.org/10.1016/j.icarus.2020.114099

Haberle, R. M. (2015). Solar system/sun, atmospheres, evolution of atmospheres | planetary atmospheres: Mars. In G. R. North, J. Pyle, & F. Zhang (Eds.), *Encyclopedia of atmospheric sciences (second edition)* (Second Edition, pp. 168–177). Academic Press. https://doi.org/https://doi.org/10.1016/B978-0-12-382225-3.00312-1

Haberle, R. M., McKay, C. P., Schaeffer, J., Cabrol, N. A., Grin, E. A., Zent, A. P., & Quinn, R. (2001). On the possibility of liquid water on present-day mars. *Journal of Geophysical Research: Planets*, *106*(E10), 23317–23326. https://doi.org/https://doi.org/10.1029/2000JE001360

Hess, S. L., Ryan, J. A., Tillman, J. E., Henry, R. M., & Leovy, C. B. (1980). The annual cycle of pressure on mars measured by viking landers 1 and 2. *Geophysical Research Letters*, *7*(3), 197–200. https://doi.org/https://doi.org/10.1029/GL007i003p00197

Holtslag, A. A. M., & Boville, B. A. (1993). Local versus nonlocal boundary-layer diffusion in a global climate model. *Journal of Climate*, *6*(10), 1825–1842. https://doi.org/https://doi.org/10.1175/1520-0442(1993)006<1825:LVNBLD>2.0.CO;2

Hu, R., Cahoy, K., & Zuber, M. T. (2012). Mars atmospheric co2 condensation above the north and south poles as revealed by radio occultation, climate sounder, and laser ranging observations. *Journal of Geophysical Research: Planets*, *117*(E7). https://doi.org/https://doi.org/10.1029/2012JE004087

Jacobson, M. Z. (2005). *Fundamentals of atmospheric modeling* (2nd ed.). Cambridge University Press. https://doi.org/10.1017/CBO9781139165389

James, P. B., Cantor, B. A., & Davis, S. (2001). Mars orbiter camera observations of the martian south polar cap in 1999–2000. *Journal of Geophysical Research: Planets*, *106*(E10), 23635–23652.

James, P. B., Kieffer, H. H., & Paige, D. A. (1992). The seasonal cycle of carbon dioxide on mars. *Mars*, 934–968.

Klein, F., Grozeva, N. G., & Seewald, J. S. (2019). Abiotic methane synthesis and serpentinization in olivine-hosted fluid inclusions. *Proceedings of the National Academy of Sciences*, *116*(36), 17666–17672. https://doi.org/10.1073/pnas.1907871116

Kok, J. F., Parteli, E. J. R., Michaels, T. I., & Karam, D. B. (2012). The physics of wind-blown sand and dust. *Reports on Progress in Physics*, *75*(10), 106901. https://doi.org/10.1088/0034-4885/75/10/106901

Korablev, O., Vandaele, A., & Montmessin, F. (2019). No detection of methane on mars from early exomars trace gas orbiter observations. *Nature*. https://doi.org/10.1038/s41586-019-1096-4

Krasnopolsky, V. A., Maillard, J. P., & Owen, T. C. (2004). Detection of methane in the martian atmosphere: Evidence for life? *Icarus*, *172*(2), 537–547. https://doi.org/https://doi.org/10.1016/j.icarus.2004.07.004

Lakdawalla, E. (2019). Similarities and differences in the landing sites of ESA's and NASA's 2020 Mars rovers. *Nature Astronomy*, *3*, 190–192. https://doi.org/10.1038/s41550-019-0727-x

Lefèvre, F., & Forget, F. (2009). Observed variations of methane on mars unexplained by known atmospheric chemistry and physics. *Nature*, *460*, 720–3. https://doi.org/10.1038/nature08228

Lewis, S. R., Collins, M., Read, P. L., Forget, F., Hourdin, F., Fournier, R., Hourdin, C., Talagrand, O., & Huot, J.-P. (1999). A climate database for mars. *Journal of Geophysical Research: Planets*, *104*(E10), 24177–24194. https://doi.org/https://doi.org/10.1029/1999JE001024

Luo, Y., Mischna, M. A., Lin, J. C., Fasoli, B., Cai, X., & Yung, Y. L. (2021). Mars methane sources in northwestern gale crater inferred from back trajectory modeling [e2021EA001915 2021EA001915]. *Earth and Space Science*, *8*(11), e2021EA001915. https://doi.org/https://doi.org/10.1029/2021EA001915

Mahaffy, P. R., Webster, C. R., Cabane, M., Conrad, P. G., Coll, P., Atreya, S. K., Arvey, R., Barciniak, M., Benna, M., Bleacher, L., Brinckerhoff, W. B., Eigenbrode, J. L., Carignan, D., Cascia, M., Chalmers, R. A., Dworkin, J. P., Errigo, T., Everson, P., Franz, H., . . . Mumm, E. (2012). The Sample Analysis at Mars Investigation and Instrument Suite., *170*(1-4), 401–478. https://doi.org/10.1007/s11214-012-9879-z

Makar, P. A., Fuentes, J. D., Wang, D., Staebler, R. M., & Wiebe, H. A. (1999). Chemical processing of biogenic hydrocarbons within and above a temperate deciduous forest. *Journal of Geophysical Research: Atmospheres*, *104*(D3), 3581–3603. https://doi.org/https://doi.org/10.1029/1998JD100065

Malin, M. C., Bell III, J. F., Cantor, B. A., Caplinger, M. A., Calvin, W. M., Clancy, R. T., Edgett, K. S., Edwards, L., Haberle, R. M., James, P. B., Lee, S. W., Ravine, M. A., Thomas, P. C., & Wolff, M. J. (2007). Context camera investigation on board the mars reconnaissance orbiter. *Journal of Geophysical Research: Planets*, *112*(E5). https://doi.org/https://doi.org/10.1029/2006JE002808

Marti, J., & Mauersberger, K. (1993). A survey and new measurements of ice vapor pressure at temperatures between 170 and 250k. *Geophysical Research Letters*, *20*(5), 363–366. https://doi.org/https://doi.org/10.1029/93GL00105

McEwen, A. S., Eliason, E. M., Bergstrom, J. W., Bridges, N. T., Hansen, C. J., Delamere, W. A., Grant, J. A., Gulick, V. C., Herkenhoff, K. E., Keszthelyi, L., Kirk, R. L., Mellon, M. T., Squyres, S. W., Thomas, N., & Weitz, C. M. (2007). Mars reconnaissance orbiter's high resolution imaging science experiment (hirise). *Journal of Geophysical Research: Planets*, *112*(E5). https://doi.org/https://doi.org/10.1029/2005JE002605

Millour, E., Forget, F., Spiga, A., Vals, M., Zakharov, V., Navarro, T., Montabone, L., Lefevre, F., Montmessin, F., Chaufray, J.-Y., Lopez-Valverde, M., Gonzalez-Galindo, F., Lewis, S., Read, P., Desjean, M.-C., & MCD/GCM Development Team. (2017). The Mars Climate Database (MCD version 5.3). *EGU General Assembly Conference Abstracts*, 12247.

Mischna, M. A., Allen, M., Richardson, M. I., Newman, C. E., & Toigo, A. D. (2011). Atmospheric modeling of mars methane surface releases [Methane on Mars: Current Observations, Interpretation and Future Plans]. *Planetary and Space Science*, *59*(2), 227–237. https://doi.org/https://doi.org/10.1016/j.pss.2010.07.005

Moores, J. E., Gough, R., Martinez, G. M., Meslin, P.-Y., Smith, C., Atreya, S., Mahaffy, P., Newman, C., & Webster, C. (2019a). Methane seasonal cycle at gale crater on mars consistent with regolith adsorption and diffusion. *Nature Geoscience*. https://doi.org/10.1038/s41561-019-0313-y

Moores, J. E., King, P. L., Smith, C. L., Martinez, G. M., Newman, C. E., Guzewich, S. D., Meslin, P.-Y., Webster, C. R., Mahaffy, P. R., Atreya, S. K., & Schuerger, A. C. (2019b). The methane diurnal variation and microseepage flux at gale crater, mars as constrained by the exomars trace gas orbiter and curiosity observations. *Geophysical Research Letters*, *46*(16), 9430–9438. https://doi.org/https://doi.org/10.1029/2019GL083800

Moores, J. E., Sapers, H. M., Oehler, D., Newman, C., & Whyte, L. (2021). High-frequency near-surface gas measurement: An opportunity to solve puzzles in planetary atmospheric processes in Martian Methane and beyond. *Bulletin of the AAS*, *53*(4). https://baas.aas.org/pub/2021n4i125

Mumma, M. J., Villanueva, G. L., Novak, R. E., Hewagama, T., Bonev, B. P., DiSanti, M. A., Mandell, A. M., & Smith, M. D. (2009). Strong release of methane on mars in northern summer 2003. *Science*, *323*(5917), 1041–1045. https://doi.org/10.1126/science.1165243

Nasa curiosity location map. (2021). Retrieved August 16, 2023, from https://mars.nasa.gov/maps/location/?mission=Curiosity

Neary, L., & Daerden, F. (2018). The gem-mars general circulation model for mars: Description and evaluation. *Icarus*, *300*, 458–476. https://doi.org/https://doi.org/10.1016/j.icarus.2017.09.028

Newman, C. E., De La Torre Juarez, M., Pla-Garcia, J., Bertrand, T., Kahre, M., Wilson, R., Daerden, F., Neary, L., Lewis, S., Forget, F., Spiga, A., Sullivan, R., Richardson, M., Sanchez-Lavega, A., Viúdez-Moreiras, D., Chide, B., & Rodriguez-Manfredi, J. (2020). Multi-model meteorological and aeolian predictions for Mars 2020 and the Jezero crater region. *AAS/Division for Planetary Sciences Meeting Abstracts*, *52*, Article 308.04, 308.04.

Oehler, D. Z., & Etiope, G. (2017). Methane seepage on mars: Where to look and why [PMID: 28771029]. *Astrobiology*, *17*(12), 1233–1264. https://doi.org/10.1089/ast.2017.1657

Pál, B., Kereszturi, Á., Forget, F., & Smith, M. D. (2019). Global seasonal variations of the near-surface relative humidity levels on present-day mars. *Icarus*, *333*, 481–495. https://doi.org/https://doi.org/10.1016/j.icarus.2019.07.007

Petrosyan, A., Galperin, B., Larsen, S. E., Lewis, S. R., Määttänen, A., Read, P. L., Renno, N., Rogberg, L. P. H. T., Savijärvi, H., Siili, T., Spiga, A., Toigo, A., & Vázquez, L. (2011). The martian atmospheric boundary layer. *Reviews of Geophysics*, *49*(3). https://doi.org/https://doi.org/10.1029/2010RG000351

Read, P. L., Galperin, B., Larsen, S. E., Lewis, S. R., Määttänen, A., Petrosyan, A., Rennó, N., Savijärvi, H., Siili, T., Spiga, A., & et al. (2017). The martian planetary boundary layer. In R. M. Haberle, R. T. Clancy, F. Forget, M. D. Smith, & R. W. Zurek (Eds.), *The atmosphere and climate of mars* (pp. 172–202). Cambridge University Press. https://doi.org/10.1017/9781139060172.007

Sandford, S. A. (2008). Terrestrial analysis of the organic component of comet dust [PMID: 20636089]. *Annual Review of Analytical Chemistry*, *1*(1), 549–578. https://doi.org/10.1146/annurev.anchem.1.031207.113108

Sapers, H., Baker, M., Edgett, K., Fey, D., Kalucha, H., Kloos, J., Lemmon, M., Newman, C., & Moores, J. (2021a). *No evidence of saltation-mediated triboluminescence at gale crater, mars* [GAC-MAC 2021 London Join Annual Meeting]. https://www.erudit.org/en/journals/geocan/2021-v48-n4-geocan06846/1087186ar.pdf

Sapers, H., Moores, J. E., Banfield, D., Oehler, D. Z., Daly, M. G., Lange, C. F., Onstott, T. C., Grandmont, F., & Choi, E. (2021b). The Martian Atmospheric Gas Evolution (MAGE) Experiment: Off-Axis Integrated Cavity-enhanced Output Spectrometer (OA-ICOS) [https://baas.aas.org/pub/2021n4i385]. *Bulletin of the AAS*, *53*(4).

Savijärvi, H. (1995). Mars boundary layer modeling: Diurnal moisture cycle and soil properties at the viking lander 1 site. *Icarus*, *117*(1), 120–127. https://doi.org/https://doi.org/10.1006/icar.1995.1146

Schorghofer, N., & Edgett, K. S. (2006). Seasonal surface frost at low latitudes on mars. *Icarus*, *180*(2), 321–334. https://doi.org/https://doi.org/10.1016/j.icarus.2005.08.022

Smith, D. E., Zuber, M. T., Frey, H. V., Garvin, J. B., Head, J. W., Muhleman, D. O., Pettengill, G. H., Phillips, R. J., Solomon, S. C., Zwally, H. J., Banerdt, W. B., Duxbury, T. C., Golombek, M. P., Lemoine, F. G., Neumann, G. A., Rowlands, D. D., Aharonson, O., Ford, P. G., Ivanov, A. B., … Sun, X. (2001). Mars orbiter laser altimeter: Experiment summary after the first year of global mapping of mars. *Journal of Geophysical Research: Planets*, *106*(E10), 23689–23722. https://doi.org/https://doi.org/10.1029/2000JE001364

Smith, M. D. (2002). The annual cycle of water vapor on mars as observed by the thermal emission spectrometer. *Journal of Geophysical Research: Planets*, *107*(E11), 25-1-25–19. https://doi.org/https://doi.org/10.1029/2001JE001522

Smith, P. H., Tamppari, L., Arvidson, R., Bass, D., Blaney, D., Boynton, W. V., Carswell, A., Catling, D., Clark, B., Duck, T., et al. (2009). H2o at the phoenix landing site. *Science*, *325*(5936), 58–61.

Stroud, C., Makar, P., Karl, T., Guenther, A., Geron, C., Turnipseed, A., Nemitz, E., Baker, B., Potosnak, M., & Fuentes, J. (2005). Role of canopy-scale photochemistry in modifying biogenic-atmosphere exchange of reactive terpene species: Results from the celtic field study. *Journal of Geophysical Research-Atmospheres*, *110*, -. https://doi.org/10.1029/2005jd005775

Taylor, P. A., Li, P.-Y., Michelangeli, D. V., Pathak, J., & Weng, W. (2007). Modelling dust distributions in the atmospheric boundary layer on mars. In A. Baklanov

& B. Grisogono (Eds.), *Atmospheric boundary layers: Nature, theory and applications to environmental modelling and security* (pp. 149–172). Springer New York. https://doi.org/10.1007/978-0-387-74321-9_11

Thøgersen, J., Bak, E. N., Finster, K., Nørnberg, P., Jakobsen, H. J., & Knak Jensen, S. J. (2019). Light on windy nights on mars: A study of saltation-mediated ionization of argon in a mars-like atmosphere. *Icarus*, *332*, 14–18. https://doi.org/https://doi.org/10.1016/j.icarus.2019.06.025

Viscardy, S., Daerden, F., & Neary, L. (2016). Formation of layers of methane in the atmosphere of mars after surface release. *Geophysical Research Letters*, *43*(5), 1868–1875. https://doi.org/https://doi.org/10.1002/2015GL067443

Wagner, W., Riethmann, T., Feistel, R., & Harvey, A. H. (2011). New Equations for the Sublimation Pressure and Melting Pressure of H2O Ice Ih. *Journal of Physical and Chemical Reference Data*, *40*(4), 043103. https://doi.org/10.1063/1.3657937

Walters, M. (2023). Methane vertical diffusion. https://doi.org/10.5281/zenodo.8253944

Wang, H., Saidel, M., Richardson, M. I., Toigo, A. D., & Battalio, J. M. (2023). Martian dust storm distribution and annual cycle from mars daily global map observations. *Icarus*, *394*, 115416. https://doi.org/https://doi.org/10.1016/j.icarus.2022.115416

Webster, C., Mahaffy, P. R., Atreya, S. K., Flesch, G. J., Farley, K. A., Team, M. S., Kemppinen, O., Bridges, N., Johnson, J. R., & Moores, J. E. (2013). Low upper limit to methane abundance on mars. *Science*, *342*(6156), 355–357. https://doi.org/10.1126/science.1242902

Webster, C., Mahaffy, P. R., Atreya, S. K., Flesch, G. J., Mischna, M. A., Meslin, P.-Y., Farley, K. A., Conrad, P. G., Christensen, L. E., Pavlov, A. A., Martín-

Torres, J., Zorzano, M.-P., McConnochie, T. H., Owen, T., Eigenbrode, J. L., Glavin, D. P., Steele, A., Malespin, C. A., Archer, P. D., … the MSL Science Team. (2015). Mars methane detection and variability at gale crater. *Science*, *347*(6220), 415–417. https://doi.org/10.1126/science.1261713

Webster, C., Mahaffy, P. R., Atreya, S. K., Moores, J. E., Flesch, G. J., Malespin, C., McKay, C. P., Martinez, G., Smith, C. L., Martin-Torres, J., Gomez-Elvira, J., Zorzano, M.-P., Wong, M. H., Trainer, M. G., Steele, A., Archer, D., Sutter, B., Coll, P. J., Freissinet, C., … Vasavada, A. R. (2018). Background levels of methane in mars’ atmosphere show strong seasonal variations. *Science*, *360*(6393), 1093–1096. https://doi.org/10.1126/science.aaq0131

Webster, Mahaffy, Paul R., Pla-Garcia, Jorge, Rafkin, Scot C. R., Moores, John E., Atreya, Sushil K., Flesch, Gregory J., Malespin, Charles A., Teinturier, Samuel M., Kalucha, Hemani, Smith, Christina L., Viúdez-Moreiras, Daniel, & Vasavada, Ashwin R. (2021). Day-night differences in mars methane suggest nighttime containment at gale crater. *A&A*, *650*, A166. https://doi.org/10.1051/0004-6361/202040030

Williams, D. (2023). Mars fact sheet. https://nssdc.gsfc.nasa.gov/planetary/factsheet/marsfact.html

Wong, A.-S., Atreya, S. K., & Encrenaz, T. (2003). Chemical markers of possible hot spots on mars. *Journal of Geophysical Research: Planets*, *108*(E4). https://doi.org/https://doi.org/10.1029/2002JE002003

Zhang, X., Berkinsky, D., Markus, C. R., Chitturi, S. R., Grieman, F. J., Okumura, M., Luo, Y., Yung, Y. L., & Sander, S. P. (2022). Reaction of methane and uv-activated perchlorate: Relevance to heterogeneous loss of methane in the atmosphere of mars. *Icarus*, *376*, 114832. https://doi.org/https://doi.org/10.1016/j.icarus.2021.114832